Main Manuscript for

Structural Insights into Biased Signaling at Chemokine Receptor CCR7

Kotaro Tanaka[1], Kouki Nishikawa[2], Yuki Shiimura[3,4],
Yoshinori Fujiyoshi[1], and Naotaka Tsutsumi[1*]

[1] Advanced Research Initiative, Institute of Integrated Research, Institute of Science Tokyo, Bunkyo, Tokyo, Japan.
[2] Joint Research Course for Advanced Biomolecular Characterization, Faculty of Agriculture, Tokyo University of Agriculture and Technology, Fuchu, Tokyo, Japan.
[3] Division of Molecular Genetics, Institute of Life Science, Kurume University, Fukuoka, Japan.
[4] Department of Cell Biology, Graduate School of Medicine, Kyoto University, Kyoto, Japan.

***Corresponding author**: Naotaka Tsutsumi
Email: tsutsumi.naotaka@tmd.ac.jp

Author contributions:
KT: Data Curation (equal), Formal Analysis (lead), Investigation (supporting), Methodology (equal), Software (lead), Validation (equal), Visualization (equal), Writing – Original Draft (supporting), Writing – Review & Editing (supporting). KN: Data Curation (supporting), Investigation (supporting), Writing – Review & Editing (supporting). YS: Methodology (supporting), Writing – Review & Editing (supporting). YF: Funding acquisition (lead), Methodology (equal), Resource (lead), Supervision (equal), Writing – Review & Editing (supporting). NT: Conceptualization (lead), Data Curation (equal), Formal Analysis (supporting),

Funding Acquisition (supporting), Investigation (lead), Methodology (equal), Project Administration (lead), Resources (supporting), Software (supporting), Supervision (equal), Validation (equal), Visualization (equal), Writing – Original Draft (lead), Writing – Review & Editing (lead).

Competing interests:

The authors declare no competing interests.

Classification:

Biological Sciences

Biophysics and Computational Biology

Keywords:

CCR7, Chemokine, Cryo-EM, MD Simulations, Signaling Bias

This PDF file includes:

Main Text

Figures 1 to 6

Abstract：

CC chemokine receptor 7 (CCR7), which orchestrates adaptive immunity, exhibits a phenomenon known as biased agonism. CCL19 induces robust G protein signaling and β-arrestin recruitment, leading to transient signaling. In contrast, CCL21 preferentially activates G protein pathways with minimal arrestin engagement, resulting in sustained signaling and differential functional outcomes. Here, we present the cryo-EM structures of the human CCR7-G_i complex with either CCL19 or CCL21. The structures reveal that while both engage a conserved orthosteric pocket, they adopt markedly distinct binding poses. Notably, the compact 30s loop of CCL21 inserts deeply into the receptor's extracellular vestibule, whereas the corresponding loop of CCL19 rests atop extracellular loop 2. Molecular dynamics simulations further reveal that these distinct binding modes induce differential intracellular dynamics, linked to the rotameric state of Y83. We demonstrate that CCL19 stabilizes a flexible conformational ensemble with a highly dynamic Helix 8, creating a lateral opening favorable for GPCR kinase engagement. Conversely, CCL21 restricts this flexibility, locking the receptor in a state that precludes kinase interaction while maintaining G protein coupling. These findings provide key insights into the structural basis of biased agonism at CCR7 and establish a foundation for rational design of pathway-selective immunomodulators.

Significance statement:

Chemokine receptor CCR7 directs immune cell migration by activating distinct signaling pathways in response to CCL19 and CCL21, a phenomenon known as biased agonism. The structural basis for this divergence has been unclear. By combining cryo-electron microscopy enabled by a robust mammalian protein production system with molecular dynamics simulations, we reveal that although both ligands stabilize similar G protein-bound conformations, they drive distinct receptor dynamics. We demonstrate that CCL19 induces a flexible intracellular conformation necessary for recruiting regulatory kinases, whereas CCL21 locks the receptor in a state that precludes this interaction. This "dynamic selection" model resolves a fundamental paradox in chemokine biology, highlighting the critical role of protein dynamics in signal transduction and providing a blueprint for designing precision immunotherapeutics.

Main Text

Introduction

Adaptive immunity relies on the precise spatiotemporal orchestration of immune cell positioning and activation to mount effective responses against pathogens and malignant cells while maintaining self-tolerance (1, 2). Central to this process is CC chemokine receptor 7 (CCR7) (SI Appendix, Fig. S1A), a G protein-coupled receptor (GPCR) that governs the trafficking of various T cells, mature dendritic cells (DCs), and B cells to secondary lymphoid organs (SLOs) (3–7). Its two endogenous ligands, CC chemokine ligand 19 (CCL19) and 21 (CCL21), form chemotactic gradients within SLOs to guide CCR7-expressing cells (8–11). This homing mechanism is essential for bringing naïve T cells into close proximity with antigen-presenting DCs within the T cell zones of SLOs, a prerequisite for T cell priming and the initiation of antigen-specific immunity (12). Given its pivotal role, the CCR7 axis is a critical therapeutic target for a broad spectrum of human pathologies (13–15). Hyperactivation of CCR7 signaling promotes the metastasis of various cancers to lymph nodes and contributes to autoimmune disorders, suggesting that antagonists could be beneficial. Conversely, insufficient CCR7 activity can impair immune surveillance and vaccine efficacy, highlighting the potential utility of precisely tuned agonists.

However, effectively targeting this axis is complicated by the phenomenon of biased agonism, for which the CCR7 system is a paradigmatic example in the chemokine family (16). Although both ligands engage the same receptor, they induce strikingly different downstream signaling profiles and cellular responses (SI Appendix, Fig. S1B). While sharing a structurally conserved core chemokine domain, CCL21 possesses a unique, highly basic C-terminal tail absent in CCL19 (SI Appendix, Fig. S1C). This tail facilitates binding to glycosaminoglycans (GAGs) on cell surfaces and in the extracellular matrix, which is crucial for establishing stable chemotactic gradients and facilitating haptotaxis (17–19). Functionally, CCL19 is a potent inducer of both G protein activation and β-arrestin recruitment. This process is mediated by receptor phosphorylation via GPCR kinases (GRKs), specifically GRK3 and GRK6, leading to potent but transient G protein signaling characterized by rapid receptor desensitization and internalization (20–22). In contrast, CCL21 activates G protein signaling at levels comparable to, or slightly

105 weaker than, those of CCL19, but inefficiently recruits β-arrestin following phosphorylation only
106 by GRK6 and causes minimal internalization (19–22). This differential regulation is physiologically
107 crucial. The acute nature of CCL19 signaling may facilitate localized cellular activation and precise
108 positioning within SLOs, whereas the sustained signaling induced by CCL21, combined with GAG-
109 regulated localization, is thought to be essential for establishing the stable, long-range
110 chemotactic gradients required for guiding cell migration over distances (18, 23–25).

111 Despite its profound physiological importance, the mechanism by which these two
112 distinct chemokines elicit biased signaling through CCR7 has been a long-standing enigma (26).
113 Understanding the molecular mechanisms underlying this bias requires elucidating how ligand
114 binding translates into distinct receptor conformations that selectively engage G proteins versus
115 GRKs and arrestins. While the crystal structure of inactive-state CCR7 bound to the small-
116 molecule intracellular antagonist Cmp2105 has provided valuable insights into inhibitor binding
117 (15), the structural underpinnings of its activation by endogenous chemokines have remained
118 elusive.

119 Here, we report the cryo-electron microscopy (cryo-EM) structures of human CCR7 in
120 complex with CCL19 and CCL21, each stabilized in an active conformation by the heterotrimeric
121 inhibitory G protein (G_i). These structures reveal distinct ligand binding modes and differential
122 receptor conformations induced by the two chemokines. The structures illustrate a unique
123 mechanism of receptor activation shared within the CCR7-like chemokine receptor subfamily.
124 Concurrently, while the overall G_i binding mode is similar, subtle conformational differences are
125 observed in intracellular regions not directly involved in G_i binding, such as ICL1, which may
126 provide insights into the distinct downstream signaling profiles. Motivated by these distinctions
127 in ligand recognition and receptor conformation, we performed molecular dynamics (MD)
128 simulations to detail the dynamic basis for these structural distinctions after G protein
129 dissociation. These simulations revealed substantial differences in receptor conformational
130 equilibria, especially in Helix 8 (H8), that might influence GRK recruitment. This study elucidates
131 the structural basis for G protein activation by two distinct chemokines, providing fundamental
132 insights into the mechanism of biased agonism at CCR7 and offering a structural template for the
133 rational design of pathway-selective agonists.

134

135 **Results**

136 **Preparation and overall architecture of the active CCR7-G_i complexes**

137 To elucidate the structural basis of CCR7 signaling, we utilized a robust strategy to
138 assemble stable, active-state complexes for cryo-EM (Fig. 1 and Methods). We employed a
139 temporally controlled expression system in tetracycline-inducible Expi293F (Expi293Fi) cells,
140 ensuring the expression of an engineered G_i heterotrimer prior to the induced expression of
141 human CCR7 in order to maximize the receptor stability and the efficiency of complex formation
142 (Fig. 1A). The G_i complex incorporated a single-chain Gγ-Gα_i fusion (27), wherein the Gα_i
143 contained dominant negative mutations (28), for enhanced stability. Additionally, the receptor
144 and G protein were non-covalently tethered using the NanoBiT system (LgBiT fused to CCR7 and
145 HiBiT fused to Gβ) (29, 30). The stable, ligand-free CCR7-G_i complex further stabilized by the
146 fiducial marker scFv16 (31) was purified, and the final signaling complexes were formed by adding
147 separately purified full-length CCL19 or CCL21, yielding viable samples for cryo-EM analysis (Fig.
148 1B-D and SI Appendix, Fig. S1D-E).

149 Single-particle cryo-EM analysis of the samples yielded high-resolution maps, achieving
150 nominal resolutions of 3.0 Å for the CCL19-CCR7-G_i-scFv16 complex and 3.2 Å for the CCL21-
151 CCR7-G_i-scFv16 complex (Fig. 2A, and SI Appendix, Table S1 and Fig. S2-S4). During 3D
152 classification, we observed structural heterogeneity related to post-translational modifications
153 (glycosylation at N36 and N292 of CCR7) and weak densities suggesting partial ordering of the
154 proximal CCL21 C-terminal tail. However, as these classes represented minor populations and
155 exhibited lower local resolution at the core interface, we focused on the most homogeneous
156 particle subsets to accurately define the primary ligand binding modes.

157 The overall architecture of the complexes resembles previously reported GPCR-G protein
158 structures, characterized by the canonical insertion of the Gα_i-α5 helix into the receptor's
159 cytoplasmic core (Fig. 2A-C). The seven-transmembrane (7TM) conformations of CCR7 in the two
160 structures are essentially identical, with a Cα root-mean-square deviation (RMSD) of 0.36 Å. They
161 also exhibit a highly similar docking mode for the G_i heterotrimer (Cα RMSD of 1.48 Å). Strikingly,

162 however, the chemokines themselves adopt distinct orientations, reflected in a substantial Cα
163 RMSD of 4.31 Å when the complexes are aligned based on the receptor (Fig. 2B).
164
165 **A unique mode of TM6 movement during CCR7 activation**
166 To understand the conformational changes associated with CCR7 activation, we
167 compared the CCL19-bound active-state structure with the inactive CCR7 structure bound to the
168 intracellular antagonist Cmp2105 (15) to elucidate the general mode of activation in comparison
169 with other chemokine receptor systems (Fig. 2C). Both CCL19 and CCL21 induce a similar global
170 conformational rearrangement in CCR7, creating a cytoplasmic cavity to accommodate the G
171 protein.
172 The most prominent feature of this transition is the outward movement of
173 transmembrane helix 6 (TM6). Unlike the canonical hinge-like pivot observed in most class A
174 GPCRs, including CCR2 and CXCR2 (32, 33), CCR7 exhibits a predominantly parallel outward shift
175 of TM6 by 3-4 Å (Fig. 2D). In CCR7, the entire TM6 helix, from its extracellular end to its
176 intracellular tip, moves laterally as a semi-rigid unit away from the receptor's central axis. This
177 mode of activation is similar to that observed in its paralog, CCR6 (34% sequence identity), which
178 also shows a ~5 Å global shift (34).
179 These distinct activation modes correlate with the presence or absence of the critical
180 $W^{6.48}$ residue within the CWxP motif (superscripts denote Ballesteros-Weinstein numbering) (Fig.
181 2D). In most class A GPCRs, $W^{6.48}$ acts as a rotamer "toggle switch," initiating conformational
182 changes that displace the intracellular half of TM6 (33, 35). In CCR7 and CCR6, this tryptophan is
183 replaced by glutamine ($Q^{6.48}$). The absence of the bulky tryptophan side chain likely enables the
184 rigid-body movement of TM6, suggesting a subclass-specific activation mechanism initiated by
185 sensing the steric bulk of the large, proteinaceous chemokine ligands rather than relying on the
186 canonical toggle switch.
187
188 **Distinct binding modes of CCL19 and CCL21 dictated by CRS3 interactions**
189 The most pronounced differences between the two active complexes are found at the
190 extracellular ligand-recognition interface. Strikingly, the core domain of CCL21 is globally rotated

191 by 17.6° relative to CCL19 when viewed from the side of the receptor (Fig. 3A). This rotation
192 results in significantly altered interaction interfaces, with larger buried surface areas for CCL21
193 (1,640 $Å^2$) compared to CCL19 (1,380 $Å^2$).

194 Chemokine recognition generally follows an expanded "two-site" model (36), involving
195 interactions across several chemokine recognition sites (CRS): CRS1 (receptor N-
196 terminus/chemokine core), CRS1.5 (receptor N-loop and ECL3/chemokine N-loop), CRS2
197 (receptor 7TM pocket/chemokine N-terminus), and CRS3 (receptor ECL2/chemokine 30s loop)
198 (Fig. 3A). Our structures reveal that the dramatic difference in orientation stems primarily from
199 divergent interactions at CRS3.

200 Despite overall sequence conservation (32% identity, 68% similarity in the core region;
201 Fig. S1C), the 30s loops of CCL19 and CCL21 exhibit distinct sequences and conformations (Fig.
202 3B). The CCL21 loop (^{30}PSLGCSIP^{38}) is notably less bulky and more hydrophobic than the
203 corresponding loop in CCL19 (^{30}IKDGCRVP^{38}), particularly featuring L32 in CCL21 versus D32 in
204 CCL19. Consequently, CCL19's 30s loop adopts a curled conformation and rests atop CCR7-ECL2.
205 In contrast, CCL21's compact 30s loop facilitates its deeper penetration into the extracellular
206 pocket. Crucially, CCL21-L32 inserts like a wedge between the chemokine N-terminus and CCR7-
207 L212^{ECL2} (Fig. 3C, right). This deep insertion stabilizes a specific conformation of ECL2 and
208 contributes significantly to the overall rotation of CCL21.

209 In contrast to the divergent CRS3 interactions, the engagements at CRS1 and CRS2 are
210 relatively conserved. At CRS1, the chemokine bodies interact with the N-terminal region of CCR7,
211 with CCR7-F44 being the core of the tip interactions (SI Appendix, Fig. S5A). At CRS2, the N-
212 terminal loops of both chemokines penetrate the "minor orthosteric binding pocket" of CCR7
213 surrounded by TM1, TM2, TM3, TM6, and TM7, forming extensive polar and hydrophobic
214 interactions (Fig. 3C) (37). The N-terminus of CCL19 penetrates slightly deeper into the pocket
215 compared to CCL21. Specifically, the sidechain of CCL19-T2 engages Y136$^{3.32}$ at TM3, inducing a
216 subtle shift of this residue. The observed CRS2 interaction networks generally correlate with
217 reported receptor mutagenesis data (38). For example, CCR7 residues K50$^{N\text{-term}}$ and R54$^{N\text{-term}}$ are
218 located at the tip of TM1 and the center of the molecular interface, forming critical contacts with
219 the N-terminal peptides of both chemokines (Fig. 3C). This explains why the CCR7-K50A$^{N\text{-term}}$ and

220 CCR7-R54A$^{N\text{-term}}$ mutations dramatically impaired both CCL19- and CCL21-induced signaling.
221 Conversely, the CCR7-R209A^{ECL2} mutation selectively reduces CCL19-induced signaling. This
222 selectivity is structurally rationalized by the more extensive polar contacts of R209^{ECL2} with the
223 N-terminus/core of CCL19, via D4/E6 sidechains and D32 backbone, compared to CCL21 (Fig. 3C),
224 suggesting that R209^{ECL2} contributes to a specific interaction network that is more critical for
225 CCL19 recognition.

226 These distinct binding modes result in ligand-specific conformational shifts in the
227 extracellular portions of TM1, TM3, TM5, TM7, and ECL2 (Fig. 3D,E and SI Appendix, Fig. S5B).
228 Furthermore, these differences propagate to an aromatic cluster located in the middle layer of
229 the minor pocket, just beneath the chemokine N-termini (Fig. 3F, and SI Appendix, Fig. S5A).
230 Residues Y65$^{1.39}$, Y136$^{3.32}$, Y279$^{6.51}$, and Y312$^{7.39}$ exhibit distinct conformations in the inactive,
231 CCL21-bound, and CCL19-bound states, where the conformational changes in the CCL19-bound
232 state are consistently more extensive than those in the CCL21-bound state. Among these residues,
233 the Y312$^{7.39}$E mutation is known to confer a high degree of constitutive activity to CCR7 while
234 abolishing chemokine sensitivities, whereas Y312$^{7.39}$A only causes high basal activities,
235 underscoring the importance of this residue for the inactive-to-active transition (19). The
236 correlated rearrangements in the aromatic network likely contribute to the differential
237 stabilization of active-state conformations and may underlie the observed differences in general
238 signaling potency (CCL19 > CCL21) (19).
239

240 **Structural basis of CCR7 activation and core G protein interface**

241 The binding of both chemokines induces canonical conformational changes associated
242 with class A GPCR activation (35) (Fig. 4A), although with the unique features related to TM6
243 movement described earlier. The PIF-like motif (P$^{5.50}$-M$^{3.40}$-F$^{6.44}$) undergoes reorganization,
244 characterized by the movement of M144$^{3.40}$ sidechain, which induces inward and outward TM5
245 and TM6 shifts, respectively (Fig. 4A, bottom left). The immediately downstream hydrophobic
246 lock collapses upon activation, further destabilizing the inactive state (Fig. 4A, bottom center).

247 Concurrently, the sodium-binding site, which is stabilized by sodium ion coordination with
248 N76$^{1.50}$, D104$^{2.50}$, N322$^{7.49}$, and Y326$^{7.53}$ in the inactive state, collapses upon activation,

249 accompanied by the kinking of the NP$^{7.50}$xxY motif including TM7 and flipping of the Y326$^{7.53}$
250 sidechain (Fig. 4A, top right). At the same time, the DR$^{3.50}$Y motif reorganizes, such that R154$^{3.50}$
251 moves to form a bridge with Y326$^{7.53}$, stabilizing the active conformation for G protein coupling
252 (Fig. 4A, bottom right).

253 Comparison of the active states with the inactive CCR7 bound to Cmp2105 highlights the
254 structural rearrangements required for G protein engagement (Fig. 4B, top left). The outward
255 movement of TM6 and the concomitant shift of TM5 create the binding pocket for the Gα_i subunit.
256 Accompanying these TM movements, the intracellular loops undergo significant reorganization.
257 Notably, ICL2 transitions from a disordered loop in the inactive state to a stable, short α-helix
258 upon activation, which is critical for engaging the Gα subunit. Similarly, ICL3 is stabilized following
259 the displacement of TM6, contributing to the formation of the G protein interface. Cmp2105
260 stabilizes the inactive state by preventing the inactive-to-active conformational shift and
261 occupying a position that overlaps with the binding site of the Gα_i-α5 helix, directly blocking G
262 protein coupling (Fig. 4B, top right).

263 The primary interface between CCR7 and Gα_i involves the insertion of the C-terminal α5-
264 helix of Gα_i deep into the cytoplasmic cavity of the receptor (Fig. 2A-C and 4B). This interface is
265 stabilized by extensive interactions and is highly conserved between the CCL19- and CCL21-
266 bound complexes (Fig. 4B, bottom panels). The Gα_i-F(-1) [F354] sidechain is sandwiched between
267 E257$^{6.29}$ and K260$^{6.32}$, positioning the C-terminal carboxyl group for polar interactions with the
268 backbone amide at the TM7-H8 turn and the K260$^{6.32}$ sidechain. The L(-2) [L353] sidechain is
269 positioned in the hydrophobic pocket formed by TM6 residues and R154$^{3.50}$ at TM3, which is
270 further covered by L(-7) [L348]. The R154$^{3.50}$ sidechain forms polar interactions with the C(-4)
271 [C351] backbone carbonyl. Although there are several minor variations at the peripheral region
272 of the core interface, the overall interaction patterns are highly conserved.

273

274 **Subtle differences at the intracellular loops suggest distinct signaling outcomes**

275 Despite the overall similarity in G protein coupling, a detailed comparison reveals subtle
276 but notable differences in the intracellular loops between the CCL19- and CCL21-bound
277 complexes (Fig. 5A,B).

278 The conformations of ICL2 and ICL3, which form the major part of the G_i interface, are
279 essentially identical in both active structures. In the ICL2 region, the interactions between CCR7
280 residues (e.g., H165, R166) and the $G\alpha_i$ αN-β1 hinge region (e.g., R32, D193) are conserved,
281 exhibiting minor variations (Fig. 5A,B, top left panels). Similarly, the core interface mediated by
282 ICL3, TM5, and TM6 is highly conserved (Fig. 5A,B, bottom left panels).

283 In contrast, ICL1, which is less directly involved in the primary G_i interface, adopts distinct
284 loop conformations in the two complexes (Fig. 5A,B, bottom right panels). This divergence
285 appears to originate from differences in the side-chain conformation of $Y83^{1.57}$, located at the
286 cytoplasmic end of TM1. The distinct binding modes of CCL19 and CCL21 induce specific
287 rearrangements in the extracellular TMs (Fig. 3D) and the central aromatic network (Fig. 3F). This
288 network appears to function as an allosteric link, propagating these differences through the
289 helical bundle (particularly TM1), ultimately leading to the distinct rotameric states of $Y83^{1.57}$ in
290 the CCL19- versus CCL21-bound structures. These states influence the length of TM1 and
291 positioning of adjacent residues and propagate to the overall conformation of the ICL1 loop.

292 While these structural variations, particularly in ICL1, are not extensive in the static G_i-
293 coupled structures, they are particularly intriguing in the context of biased signaling. The high
294 similarity of the G_i-coupled states suggests that the mechanism underlying the differential
295 recruitment of GRKs and arrestins likely stems from differences in receptor conformations or
296 dynamics that occur after G protein activation and dissociation. Although ICL1 is not considered
297 the primary determinant of GRK binding, GRKs recognize specific conformations of the
298 intracellular loops and the receptor core to phosphorylate the receptor (39, 40). It is plausible
299 that the distinct extracellular binding modes of CCL19 and CCL21 prime the receptor to adopt
300 different conformational ensembles, including intracellular architectures other than ICL1, upon
301 G protein release.

302

303 **Molecular Dynamics simulations to probe the basis of biased signaling**

304 To investigate how the distinct ligand binding modes and the subtle intracellular
305 differences might influence receptor dynamics relevant to biased signaling, we performed six
306 independent 2.3 µs all-atom MD simulations for each complex (Fig. 5C and S6-S9). We used the

307 experimental CCL19-CCR7 and CCL21-CCR7 structures as starting points, after removing the G
308 protein and scFv16 and embedding the complexes in a lipid bilayer (SI Appendix, Fig. S6A and
309 Methods). These starting points are intended to mimic the receptor states primed for subsequent
310 signaling events, such as GRK recruitment, after initial G protein activation and dissociation.

311 During the simulations, the chemokine ligands (especially CCL19) exhibited higher
312 flexibility (SI Appendix, Fig. S6B,C), consistent with the observed cryo-EM density at the
313 chemokine region (SI Appendix, Fig. S2-S3). In contrast, the receptor core (7TM bundle) of both
314 complexes slightly deviated from the initial cryo-EM conformation, but converged to a similar
315 conformational state (SI Appendix, Fig. S6B,C and S7).

316 The most notable finding was the differential dynamics of H8 in CCR7 (Fig. 5C). In the
317 CCL19-bound state, the TM7-H8 loop exhibits higher dynamics and repositions into the receptor
318 central axis, forming a larger gap between TM6 and TM7 (Fig. 5C). This is characterized by the
319 proximity between TM2 and the TM7-H8 loop, and the H8 rotation (SI Appendix, Fig. S8). In the
320 CCL19-bound state, the Cα distance between T93$^{2.39}$ and G330$^{8.47}$ became substantially narrower
321 from 11.5 Å to approx. 6.4 Å, accompanied by a significant rotation from the cryo-EM
322 conformation (defined as H8 angle 0°) to a new stable state at approx. -28.2°. In the CCL21-bound
323 state, however, H8 remained more stable near the cryo-EM conformation with the Cα distance
324 between T93$^{2.39}$ and G330$^{8.47}$ remaining constant at approx. 11.3 Å and the rotation being less
325 pronounced rotation to approx. -14.4°.

326 These differences trace back to the formation of two distinct salt bridges: a highly stable
327 one directly linking R88$^{12.49}$ (ICL1) to D336$^{8.53}$ (H8) (present in 92% of simulation time), and a
328 second, dynamic one between R88$^{12.49}$ (ICL1) and D94$^{2.40}$ (TM2) (present in 58% of simulation
329 time) (SI Appendix, Fig. S9A, top panel, and S9B). In sharp contrast, in the CCL21-bound state,
330 while the R88$^{12.49}$-D336$^{8.53}$ bridge remained largely stable (86% formation), the crucial R88$^{12.49}$-
331 D94$^{2.40}$ bridge which brings H8 toward TM2 was almost entirely absent (9% formation).

332 This dynamic behavior in the CCL19-bound state also correlates with the different chi1
333 (χ1) angles of Y83$^{1.57}$ at the TM1 terminus (180° for CCL19 and -86° for CCL21), observed in the
334 cryo-EM structures, which remained stable in their respective states throughout the simulations
335 (SI Appendix, Fig. S9A, bottom panel, and S9C). This orientation of Y83$^{1.57}$ appeared to influence

336 the ICL1 dynamics and allosteric coupling between ICL1 and H8 (SI Appendix, Fig. 5C and S9A,D).
337 In the CCL19-bound state, the outward-facing conformation of Y83$^{1.57}$ accommodates F333$^{8.50}$
338 from H8 into the pocket near TM2, which is blocked by the inward-facing Y83$^{1.57}$ sidechain in the
339 CCL21-bound state.

340 Taken together, these results suggest that the specific intracellular domain reorganization
341 induced by CCL19, particularly the dynamic movement of H8, differs from the stable
342 conformation induced by CCL21, and likely has a differential impact on the recognition of
343 downstream effectors like GRKs. We hypothesize that the stable conformational ensemble
344 induced by CCL21, which settles into a single state lacking the deep H8 insertion (Fig. 5C, bottom
345 left panel) and thus resembling the G_i-bound conformation in the core pocket, is suboptimal for
346 GRK interaction. This "locked" state, which appears to remain competent for G protein coupling
347 but not for GRK engagement, results in G protein-biased signaling. In contrast, the
348 conformational flexibility induced by CCL19 appears to sample multiple states, in which a major
349 population representing the H8-shifted "open" state characterized by the deeper insertion of the
350 TM7-H8 loop coexists with a population lacking this insertion and thus resembling the starting
351 G_i-bound conformation (Fig. 5C, top left panel). This dynamic equilibrium, which allows the
352 sampling of both a GRK-favorable state and a G_i-favorable state, may represent the structural
353 basis for CCL19's potent, non-biased activation profile, facilitating the efficient engagement of
354 both G proteins and GRKs.
355

356 **Discussion**

357 The precise orchestration of immune cell migration by the CCL19/CCL21-CCR7 axis is
358 fundamental to adaptive immunity. This system partly relies on the biased agonism of its two
359 ligands to achieve distinct physiological outcomes, localized activation versus long-range
360 chemotaxis (18, 23, 24, 41). Our structural analyses provide a molecular framework for
361 understanding how this divergence is achieved.

362 The cryo-EM structures reveal a marked divergence in ligand recognition, primarily
363 dictated by interactions at the CRS3 interface (Fig. 3). The deep, hydrophobic engagement of the
364 CCL21 30s loop contrasts sharply with the shallower binding of CCL19 loop, illustrating how the

365 sequence variations in flexible chemokine loops can alter the overall binding topology.
366 Furthermore, our analysis highlights that CCR7 employs a non-canonical, rigid-body movement
367 of TM6 during activation (Fig. 2), likely facilitated by the absence of the canonical $W^{6.48}$ toggle
368 switch. This mechanism suggests a specialized adaptation within this receptor subfamily for
369 transducing signals from protein ligands.

370 The central paradox of CCR7 bias is that both ligands induce highly similar G_i-coupled
371 conformations (Fig. 5A,B) yet elicit vastly different downstream responses regarding
372 desensitization (22). Our MD simulations suggest that the mechanism of bias lies not in the initial
373 G protein engagement, but in the receptor dynamics that follow G protein dissociation, revealing
374 that CCL19 induces a flexible ensemble capable of adopting a widely "open" H8 state, whereas
375 CCL21 stabilizes a single, "locked" G_i-bound-like state (Fig. 5C).

376 Structural comparisons with other GPCR-GRK complexes underscore the importance of
377 this CCL19-induced "open," H8-shifted state (Fig. 6). Cryo-EM structures of neurotensin receptor
378 1 (NTSR1) and Rhodopsin (Rho) reveal that the binding modes of the Gα C-terminal α5 helix and
379 the GRK N-terminal α-helix (αN) are mutually exclusive (39, 40, 42, 43) (Fig. 6A, B). While the Gα-
380 α5 helix requires its deeper insertion towards the receptor core, the GRK-αN helix exhibits a
381 shallower insertion and follows a distinct trajectory, exiting through the lateral gap formed
382 between TM6 and the TM7-H8 loop. This suggests a general mechanism where efficient GRK
383 recognition requires not only a sufficiently wide lateral opening between TM6 and the TM7-H8
384 loop, but perhaps also a conformation that disfavors the deep re-insertion of a G protein.

385 In this context, our findings provide a compelling structural rationale for the biased
386 signaling, where the conformational flexibility of CCL19-bound CCR7 plays a key role. Its ability
387 to dynamically adopt the "open" state, in which the TM7-H8 loop itself inserts into the
388 cytoplasmic cavity (Fig. 5C), simultaneously achieves two discrete goals. It occupies the deep
389 central cavity, thus sterically hindering deep G protein re-engagement, and creates the widened
390 lateral gap favorable for initiating GRK3 engagement (a GRK2/3 subfamily member known to
391 phosphorylate CCR7) (Fig. 6C). Furthermore, this inserted TM7-H8 loop may form a novel
392 composite interaction surface for GRK recognition, as the GRK-biased small molecule SBI-553
393 does for NTSR1 (40).

394 This model explains the non-biased profile of CCL19, where the CCL19-bound CCR7
395 exhibits dynamic equilibrium that allows it to adopt both this "open," GRK-favorable state and
396 the G_i-bound-like state lacking the loop insertion, permitting efficient engagement of both
397 effector types. Conversely, the "locked" stable state stabilized by CCL21 maintains a vacant deep
398 pocket and a narrower lateral gap, while also lacking the TM7-H8 loop insertion. This
399 conformation appears to remain highly competent for G protein coupling but fails to provide the
400 steric opening or interaction surface required for efficient GRK3 engagement. This structural
401 dichotomy—a flexible ensemble of both G_i- and GRK-favorable states versus a conformationally
402 restricted, G_i-competent-only state—offers a mechanistic basis for the G protein-biased signaling
403 observed for CCL21.
404 The dynamic model aligns with their physiological roles. CCL19, by inducing
405 conformational dynamics favorable for GRK engagement, drives rapid desensitization and
406 internalization (20, 22). This transient signaling is ideally suited for the precise tuning of immune
407 function, particularly in acute cell activation and tissue development (23, 41, 44–47). In contrast,
408 the unique binding mode of CCL21 stabilizes a conformationally restricted ensemble that
409 disfavors efficient GRK3 interaction, resulting in sustained G protein signaling (20). This G protein
410 bias is essential for guiding immune cells over long distances (18, 25, 45). Moreover, the deep
411 insertion of the CCL21 30s loop may also contribute to a slower dissociation rate, further
412 supporting sustained signaling. This mechanism, combined with the known role of the CCL21 C-
413 terminal tail in establishing stable chemotactic gradients via GAG interactions (17–19), provides
414 a comprehensive explanation for its function in long-range migration and haptotaxis.
415 In conclusion, this study elucidates the structural and dynamic basis of biased agonism at
416 CCR7, demonstrating how subtle differences in ligand recognition are translated into distinct
417 physiological outcomes. Thus, exploring chemokine analogs that simultaneously modulate
418 interactions across the CRS2 and CRS3 interfaces, perhaps mimicking the specific engagement
419 profile of CCL21 but at higher affinity, might lead to G protein-biased agonists. Such molecules,
420 by potentially promoting sustained cell trafficking, could serve as adjuvants for vaccines or cancer
421 immunotherapy. This structural framework thus provides a foundation for developing novel
422 immunomodulators designed to precisely control the CCR7 signaling axis.

423

424 **Limitations of Study**

425 While the current structures and MD simulations provide significant insights into CCR7 activation
426 and mechanisms possibly linked to the biased signaling, several limitations remain. These data
427 do not directly visualize the conformations responsible for GRK or β-arrestin engagement.
428 Determining the structures of CCR7 in complex with GRKs or β-arrestins will be crucial to fully
429 elucidate the mechanisms of biased signaling. Furthermore, although we observed heterogeneity
430 related to the CCL21 C-terminal tail and potential post-translational modifications in cryo-EM
431 density, we could not resolve these features at high resolution. Further studies are needed to
432 understand their roles in CCR7 function and regulation.

433 **Materials and Methods**

434 **Mammalian cell lines and culture conditions**

435 Expi293F inducible (Expi293Fi) cells (Thermo Fisher Scientific, a component of expression system
436 kit Cat# A39251) were adopted and maintained in HE400AZ media (GMEP) supplemented with
437 10 µg/mL Blasticidin (InvivoGen) at a 20 mL culture scale. For protein expression, cells were
438 expanded with HE400AZ media up to 200 mL and then HE200 media (GMEP) supplemented with
439 GlutaMAX (Thermo Fisher Scientific) for larger volumes to reduce the total cost. Cells were
440 maintained at a density between 0.3 and 4 × 10^6/mL and shaken at 37°C and 130 rpm with 8%
441 (v/v) CO_2. Transfections were performed at a cell density of approximately 3 × 10^6/mL.

442

443 **Insect cell lines and culture conditions**

444 For scFv16 expression from *Trichoplusia ni* (Hi5) ovarian cells (Expression Systems, Cat# 94-002),
445 baculovirus was produced in *Spodoptera frugiperda* (Sf9) ovarian cells (ATCC CRL-1711)
446 maintained in Sf-900 III medium (Thermo Fisher Scientific) with 10% (v/v) FBS (Sigma-Aldrich) and
447 GlutaMAX. Hi5 cells were maintained and expanded for protein expression in ESF 921 Insect Cell
448 Culture Medium (Expression Systems). Insect cells were grown at 27°C with ambient CO_2 and
449 gentle agitation, and baculovirus infections for virus amplification and protein expression were
450 performed at a cell density of approximately 2 × 10^6/mL.

451

452 **Expression of the apo CCR7-G_i complex**

453 The expression plasmids were designed to perform induced and constitutive co-
454 expression of CCR7 and heterotrimeric G_i protein, and the coding genes were synthesized by
455 GenScript for cloning in expression plasmids. The full-length human CCR7 lacking the endogenous
456 signal peptide (UniProt ID: P32248, residues 25-378) was cloned into pcDNA5/TO vector (Thermo
457 Fisher Scientific) with the N-terminal HA secretion signal peptide followed by FLAG tag, and C-
458 terminal LgBit split NanoLuc fragment (29). Single chain human $G\gamma_2$-$G\alpha_{i1}$, where $G\alpha_{i1}$ (UniProt ID:
459 P63096, residues 2-354) with dominant negative mutations (S47N, G203A, E245A, A326S) (28)
460 was fused downstream of $G\gamma_2$ (UniProt ID: P59768) separated by 3x GSA linker (27) and cloned
461 into the pEG vector (48). Human $G\beta_1$ (UniProt ID: P62873) with C-terminal HiBit NanoLuc

462 complementation fragment and N-terminal 3C protease-cleavable 10×His tag was also cloned
463 into the pEG vector for co-expression.
464 Protein expression was performed using Expi293Fi cells as per manufacturer's
465 recommendation with modifications to use polyethyleneimine (PEI) Max (Polysciences) as a
466 transfection reagent (49), 3 mM sodium valproate and 0.4% (w/v) glucose as enhancers (50), and
467 doxycycline (Wako) as the inducer. The three plasmids were used at an approximately equal
468 weight ratio, and a total of 1 µg plasmid and 4 µg PEI per 1 mL cell culture were mixed in HE400AZ
469 media and incubated for 15 min at room temperature before transfecting the Expi293Fi cells.
470 One day after transfection, the enhancers were added, and after an additional 24 hours at 37°C
471 for initial G_i expression, the CCR7 expression was induced by adding 8 µM doxycycline. The
472 culture flask was transferred to a 30°C incubator and shaken for 48 hours. The cells were
473 harvested, washed once with phosphate-buffered saline (PBS), and stored at -30°C. 200 mL
474 Expi293Fi culture typically yields approximately 5 grams of cell pellet.
475
476 **Expression and purification of CCL19, CCL21, and scFv16**
477 CCL19 and CCL21 were expressed from Expi293Fi cells but with constitutive expression
478 using a standard CMV promoter, and the coding genes were synthesized by GenScript. Full-length
479 CCL19 (UniProt ID: Q99731) and CCL21 (UniProt ID: O00585) were each fused to the C-terminal
480 6×His-tagged human IgG1 Fc via the GSGSGSAAA linker, HRV 3C protease site (LEVLFQGP), and
481 GSDGSGSGS linker analogous to the construct previously used to prepare the chemokine domain
482 of CX_3CL1 (51) but cloned into pD649 transient expression vector (ATUM) (52) instead of the
483 BacMam transfer vector (53). Transfection was performed as described for the CCR7-G_i complex
484 with a 1:4 plasmid:PEI ratio, and the enhancers were added to the culture on the following day.
485 The cells were shaken in the 37°C incubator for an additional 84 hours, and the culture
486 supernatant was collected for purification using Ni-NTA (51, 52). The Fc-tagged chemokines were
487 eluted with HEPES-buffered saline (HBS, 10 mM HEPES-Na pH 7.2 and 150 mM NaCl) containing
488 250 mM imidazole, and the Fc tag was removed by adding 2% (w/w) 3C protease, which was
489 prepared in-house. The solutions were buffer exchanged to HBS containing 10 mM imidazole,
490 flowed through Ni-NTA equilibrated with HBS containing 20 mM imidazole to remove the Fc tag,

491 and concentrated to approximately 300 µL. Due to the limited protein yields (~50 µM and ~20
492 µM for CCL19 and CCL21, respectively), the samples were supplemented with 10% (v/v) glycerol,
493 aliquoted, flash-frozen, and stored at -80°C for further use.

494 scFv16 (31) was expressed from Hi5 ovarian cells using Bac-to-Bac baculovirus expression
495 system (Thermo Fisher Scientific) and purified as reported previously (51). Briefly, the collected
496 Hi5 culture supernatant was clarified after a precipitate was formed by adding 1 mM $NiCl_2$, 5 mM
497 $CaCl_2$, and 50 mM Tris-HCl (pH 8), and then incubated with Ni-NTA to capture the C-terminal
498 6×His-tagged scFv16. The Ni-NTA resin was collected, washed with HBS containing 20 mM
499 imidazole, and eluted by increasing imidazole concentration to 250 mM. The eluate was
500 concentrated and purified using a size-exclusion chromatography column (SEC) Superdex 75
501 10/300 GL (Cytiva) equilibrated with HBS. The peak fraction was concentrated to approximately
502 640 µM, aliquoted and flash-frozen with 10% (v/v) glycerol, and stored at -80°C until future use.
503

504 **Purification of CCR7-G_i-scFv16 complexes bound to CCL19 or CCL21**

505 The ligand-free, NanoBiT-tethered CCR7-G_i-scFv16 complex was purified before the
506 chemokines were added during the final protein concentration step. Approximately 5 grams of
507 cell pellet expressing CCR7-G_i was directly solubilized for 2 hours at 4°C with 10 nmol of
508 recombinant scFv16 and nutation in a solubilization buffer consisting of HBS, 10% (w/v) glycerol,
509 1% (w/v) n-dodecyl-β-D-maltoside (DDM, Anatrace), 0.1% (w/v) lauryl maltose neopentyl glycol
510 (LMNG, Anatrace), 0.11% (w/v) cholesteryl hemisuccinate tris salt (CHS, Anatrace), cOmplete
511 protease inhibitor cocktail (Roche), and apyrase (0.2 µL, New England Biolabs). The resulting cell
512 lysate was clarified by two sequential centrifugations at 12,000 *g* for 30 minutes at 4°C. The
513 supernatant was then supplemented with 3 mM $CaCl_2$ and incubated with 1 mL of in-house anti-
514 FLAG M1 sepharose for 2 hours at 4°C. The resin was collected in a column and washed
515 sequentially, first with the solubilization buffer, then HBS containing 0.1% LMNG, 0.01% CHS, and
516 3 mM $CaCl_2$. A final wash was performed with HBS containing 0.01% LMNG, 0.001% CHS, and 3
517 mM $CaCl_2$, and the CCR7-G_i-scFv16 complex was eluted from the column with HBS buffer
518 containing 0.001% LMNG, 0.001% glyco-diosgenin (GDN, Anatrace), 0.0001% CHS, 5 mM EDTA,
519 and 100 µg/mL FLAG peptide (PH Japan). The eluate was concentrated to approximately 400 µL,

520 and 2% (w/w) of in-house 3C protease was added for overnight incubation at 4°C. The protein
521 was subjected to SEC on a Superdex 200 Increase 10/300 GL column (Cytiva) equilibrated with
522 SEC buffer consisting of HBS, 0.001% LMNG, 0.001% GDN, and 0.0001% CHS. Peak fractions were
523 collected, concentrated, and quantified, yielding approximately 0.20 mg (1.1 nmol) of the
524 purified CCR7-G_i-scFv16 complex.

525 Concurrently, frozen stocks of the chemokines CCL19 and CCL21 were thawed and
526 dialyzed against the SEC buffer using Xpress Micro Dialyzer with a 3.5 kDa molecular weight cutoff
527 (MWCO) (Scienova GmbH). To form the chemokine-bound signaling complexes, each prepared
528 chemokine was added to the purified CCR7-G_i-scFv16 in separate reactions. Specifically, CCL19
529 was added at a 1.6-fold molar excess to 0.6 nmol of CCR7-G_i-scFv16, while CCL21 was added at
530 the same molar ratio to 0.5 nmol aliquot of the ligand-free complex. Finally, each mixture was
531 concentrated to 4.5 mg/mL using 3 kDa MWCO Amicon Ultra 0.5 mL centrifugal filters for cryo-
532 EM.

533

534 **Cryo-EM grid preparation and data collection**

535 For cryo-EM analysis, a 3.5 µL aliquot of either complex was applied to a glow-discharged
536 Quantifoil R1.2/1.3 300-mesh gold grids. The grids were plunge-frozen in liquid ethane using a
537 Vitrobot Mark IV (Thermo Fisher Scientific) with a 10-sec hold period, blot force of 10, and
538 blotting time of 2-4 sec with 100% humidity at 4°C.

539 Cryo-EM data were subsequently collected using a JEOL JEM-Z320FHC electron
540 microscope operated at 300 kV, equipped with an in-column omega energy filter set to a 20 eV
541 slit width. Images were recorded on a Gatan K3 camera in correlated double sampling mode, with
542 a calibrated pixel size of 0.79 Å at the specimen. Automated data acquisition was performed using
543 SerialEM (54) with a 3 × 3 image-shift pattern and a nominal defocus range of -1.0 to -1.8 µm.
544 Each movie was recorded for 2.6 seconds, fractionated over 50 frames, yielding a total exposure
545 of 50 electrons/$Å^2$ and an exposure rate of 1 electron/$Å^2$ per frame. A total of 20,142 movies
546 (7,506 + 12,636) were collected from two grids for the CCL19-CCR7-G_i-scFv16 complex, while
547 5,968 movies (2,376 + 3,592) were collected from two grids for the CCL21-CCR7-G_i-scFv16
548 complex.

549

550 **Cryo-EM data processing**

551 The data were analyzed using cryoSPARC version 4 (55) for both signaling complexes
552 unless otherwise noted, and the data processing schemes are summarized in Fig. S2 and S3. Patch
553 motion correction and contrast transfer function (CTF) estimation were performed. Particles
554 were picked iteratively with template-based picking using a representative GPCR-G protein
555 complex and Topaz picking (56) combined with 2D classifications.

556 For the CCL19-CCR7-G_i-scFv16 complex (Fig. S2), 3,374,958 initial particles were extracted
557 and subjected to Non-uniform Refinement (NU-refine) with Global and Local CTF Refinements. A
558 representative GPCR-G protein-scFv16 complex was used as an initial reference map low-pass
559 filtered to 30 Å. 3D classification was first performed to eliminate the complex particles with poor
560 7TM density. Several rounds of Heterogeneous Refinement (Hetero-Refine) and NU-Refine were
561 performed to isolate a homogeneous subset of particles. We then utilized 3D Variability Analysis
562 (3DVA) followed by Hetero-Refine using the resulting 3DVA volumes as references. While we
563 observed heterogeneity related to glycosylation, such as at N292, we prioritized classes with the
564 best-defined chemokine core features. The resulting class was further refined using Reference-
565 Based Motion Correction (RBMC), NU-refine, and Local CTF Refinement. The selected 256,195
566 particles were subjected to the final NU-Refine, which yielded a map with a nominal resolution
567 of 3.0 Å as determined by the gold-standard Fourier shell correlation (GSFSC) at the 0.143
568 threshold.

569 For the CCL21-CCR7-G_i-scFv16 complex (Fig. S3), 1,537,777 initial particles were
570 processed similarly. After initial 2D and 3D classification, particles representing the best class and
571 minor views from the second-best class were merged and subjected to iterative rounds of NU-
572 Refine, RBMC, and Local CTF-Refine. Subsequent 3DVA-based Hetero-Refine were employed to
573 address conformational heterogeneity at the chemokine core. Notably, we identified minor
574 classes exhibiting weak or partial density corresponding to potential N-linked glycosylation at
575 N36 and N292 of CCR7, as well as ambiguous density near the extracellular surface potentially
576 representing parts of the flexible CCL21 C-terminal tail (Fig. S3A). However, these classes
577 constituted a small fraction of the dataset and displayed lower homogeneity and resolution in

578 the core chemokine-receptor interface compared to the major population. Therefore, we
579 focused on the most homogeneous subset to achieve the highest local resolution (quality or
580 modelability) of the chemokine region. After several rounds of refinement and classification, the
581 final set of 195,011 particles yielded a map with a nominal resolution of 3.2 Å determined by
582 GSFSC at 0.143 threshold.

583 The maps were sharpened with a B-factor of -60 $Å^2$ for model building, refinement and
584 visualization of the map-model correlation. For both datasets, local resolution was estimated
585 using cryoSPARC, and the maps were further sharpened using deepEMhancer for overall map
586 presentation purposes only (57). UCSF pyEM v0.5 (58) was used to plot particle viewing directions
587 on the 3D maps.

588

589 **Model building and refinement**

590 The initial models were prepared using AlphaFold3 (59), and each subunit was roughly
591 fitted into the map by real-space rigid body refinement using Phenix (60). The models were
592 subjected to iterative rounds of manual rebuilding in Coot (61) and real-space refinement using
593 Phenix. Secondary structure restraints and geometry restraints were applied during refinement.
594 The map-model correlation and refinement statistics are summarized in Table S1 and Fig. S4.
595 Figures were prepared using UCSF ChimeraX (62) and PyMOL (Schrödinger, LLC).

596

597 **Molecular dynamics simulations**

598 Input models and parameters for all-atom MD simulations of CCR7 complexed with CCL19
599 or CCL21 were generated using CHARMM-GUI (63–65). All molecules other than CCR7 and
600 CCL19/21 were stripped from the cryo-EM models. The unmodelled sidechains were manually
601 built and refined with Coot (61). The internal water molecules were placed based on the
602 estimation by HOMOLWAT (66). The unmodelled part of the N-terminus and the C-terminus of
603 CCR7 and CCL19/21 were left unmodelled, and the terminal amino groups and the carboxyl
604 groups were neutrally capped by acetylation (ACE patch) and methylamidation (CT3 patch),
605 respectively. Protonation states of the titratable residues at pH 7.0 were determined with
606 PROPKA (67). The terminal amino groups of the native N-terminus of CCL19 (G1) and CCL21 (S1)

607 were deprotonated by NGNE patch and NNEU patch, respectively (estimated pKa 5.96 and 4.51).
608 Because the NGNE patch was not available in CHARMM-GUI, a local install of CHARMM c49b2
609 (68) was used for the patching using the scripts generated by CHARMM-GUI. All the aspartic acid
610 and glutamic acid residues were negatively charged except D104$^{2.50}$ (estimated pKa 7.50 in CCR7-
611 CCL19 and 7.81 in CCR7-CCL21). All the lysine and arginine residues were positively charged. All
612 the histidine residues were neutralized by δ-nitrogen protonation. The model was embedded in
613 a rectangular lipid bilayer comprising 203 POPC molecules (102 in the upper leaflet and 101 in
614 the lower leaflet) with the orientation estimated by PPM2.0 (69). The system was solvated and
615 charge-neutralized by ~24,000 water molecules (water layers of 22.5 Å thickness on top and
616 bottom of the proteins) and 150 mM NaCl. The system dimensions and the total number of atoms
617 were 90 Å × 90 Å × 141 Å and 107,178 atoms for CCR7-CCL19, 90 Å × 90 Å × 139 Å and 105,680
618 atoms for CCR7-CCL21 (Fig. S6A). The CHARMM36m force-field parameters (70) were used for
619 the proteins, lipids, and ions. The TIP3P model was used for water.
620 MD simulations were performed using GROMACS 2024.3 (71). Each system was energy-
621 minimized using the steepest-descent algorithm for 10,000 steps. Then, six independent MD runs
622 (replicas) were performed. For each replica, the system was equilibrated and relaxed in the
623 following way. First, temperature was elevated from 0 to 100 K for 20 ps in the NVT ensemble
624 using the V-rescale thermostat (72). Temperature was further elevated from 100 K to 310.15 K
625 under the pressure of 1 bar for 400 ps in the NPT ensemble using the V-rescale thermostat and
626 the Berendsen barostat (73). During the energy minimization and the temperature elevation, the
627 x, y, z positions of the backbone heavy atoms, the x, y, z positions of the sidechain heavy atoms,
628 the z positions of the POPC phosphorous atoms, the dihedral angles about the double bond in
629 the POPC alkyl chain, were harmonically restrained to the initial configuration at the force
630 constant of 4000 kJ/mol/nm^2, 2000 kJ/mol/nm^2, 1000 kJ/mol/nm^2 and 1000 kJ/mol/rad^2,
631 respectively. Then the restraints were gradually relaxed towards 0 for 35 ns in the NPT ensemble
632 of 310.15 K and 1 bar using the V-rescale thermostat and the C-rescale barostat (74). After that,
633 the production run was performed for 2.3 μs in the NPT ensemble of 310.15 K and 1 bar using
634 the V-rescale thermostat and the C-rescale barostat at the timestep of 2 fs. Bond lengths
635 involving hydrogen atoms were constrained using the LINCS algorithm (75). Long-range

636 electrostatic interactions were calculated with the particle mesh Ewald method (76). Atomic
637 coordinates were saved every 100 ps. The simulations were carried out using the TSUBAME4.0
638 supercomputer at Institute of Science Tokyo.

639 The molecules were made 'whole' and put back into the simulation cell using the gmx
640 trjconv program in the GROMACS package. The trajectory analysis was performed using
641 MDAnalysis v2.9.0 (77) and the graphs were visualized using Matplotlib (78). To align the
642 trajectories, the corresponding cryo-EM models were used as the alignment references, which
643 are transformed so that the (x, y) origin is the center of the proteins and the z origin is the center
644 of the membrane, and the z-axis is perpendicular to the membrane (Fig. S7B).

645 In all the trajectory analysis except the ICL1 conformational analysis (Fig. S9D), the
646 trajectories were least-squares aligned to the reference models by the Cα atoms of CCR7 except
647 the flexible N-terminal (-50) and ECL2 (200-209) regions. In the ICL1 conformational analysis (Fig.
648 S9D), the trajectories were aligned by the Cα atoms of the ICL1-flanking residues of TM1 and TM2
649 (78-85, 92-99).

650 In all the trajectory analysis except the simulation time course plots, the first 1 μs of the
651 2.3 μs simulation were excluded from the analysis as the relaxation (equilibration) period,
652 because the average RMSD (Fig. S6B) and the TM helices displacements (Fig. S7A) were rapidly
653 changing in this period.

654 The MD snapshots used in the figures were selected so that the TM centroid coordinates
655 and the H8 orientation (the angle and the TM2-G330 distance) are closest to the MD average (the
656 timestep 1597.8 ns of replica #1 for CCL19-CCR7, the timestep 1236.1 ns of replica #1 for CCL21-
657 CCR7).

658 The density plots in Fig. 5C and in Fig. S9B were calculated using the Gaussian kernel
659 density estimation implemented in Scikit-learn (79).

660 **References**

661 1. D. J. Fowell, M. Kim, The spatio-temporal control of effector T cell migration. *Nat Rev*
662 *Immunol* **21**, 582–596 (2021).
663 2. H. Qi, W. Kastenmüller, R. N. Germain, Spatiotemporal basis of innate and adaptive
664 immunity in secondary lymphoid tissue. *Annu Rev Cell Dev Biol* **30**, 141–167 (2014).
665 3. M. D. Gunn, *et al.*, Mice lacking expression of secondary lymphoid organ chemokine
666 have defects in lymphocyte homing and dendritic cell localization. *J Exp Med* **189**, 451–
667 460 (1999).
668 4. R. Förster, *et al.*, CCR7 coordinates the primary immune response by establishing
669 functional microenvironments in secondary lymphoid organs. *Cell* **99**, 23–33 (1999).
670 5. K. Reif, *et al.*, Balanced responsiveness to chemoattractants from adjacent zones
671 determines B-cell position. *Nature* **416**, 94–99 (2002).
672 6. A. J. Ozga, M. T. Chow, A. D. Luster, Chemokines and the immune response to cancer.
673 *Immunity* **54**, 859 (2021).
674 7. M. Birkenbach, K. Josefsen, R. Yalamanchili, G. Lenoir, E. Kieff, Epstein-Barr virus-
675 induced genes: first lymphocyte-specific G protein-coupled peptide receptors. *J Virol*
676 **67**, 2209 (1993).
677 8. R. Yoshida, *et al.*, Molecular cloning of a novel human CC chemokine EBI1-ligand
678 chemokine that is a specific functional ligand for EBI1, CCR7. *Journal of Biological*
679 *Chemistry* **272**, 13803–13809 (1997).
680 9. M. Nagira, *et al.*, Molecular cloning of a novel human cc chemokine secondary
681 lymphoid- tissue chemokine that is a potent chemoattractant for lymphocytes and
682 mapped to chromosome 9p13. *Journal of Biological Chemistry* **272**, 19518–19524
683 (1997).
684 10. R. Förster, A. C. Davalos-Misslitz, A. Rot, CCR7 and its ligands: balancing immunity and
685 tolerance. *Nat Rev Immunol* **8**, 362–371 (2008).
686 11. I. Comerford, *et al.*, A myriad of functions and complex regulation of the
687 CCR7/CCL19/CCL21 chemokine axis in the adaptive immune system. *Cytokine Growth*
688 *Factor Rev* **24**, 269–283 (2013).
689 12. S. A. Luther, H. L. Tang, P. L. Hyman, A. G. Farr, J. G. Cyster, Coexpression of the
690 chemokines ELC and SLC by T zone stromal cells and deletion of the ELC gene in the
691 plt/plt mouse. *Proc Natl Acad Sci U S A* **97**, 12694–12699 (2000).
692 13. L. Han, L. Zhang, CCL21/CCR7 axis as a therapeutic target for autoimmune diseases. *Int*
693 *Immunopharmacol* **121** (2023).
694 14. A. Salem, M. Alotaibi, R. Mroueh, H. A. Basheer, K. Afarinkia, CCR7 as a therapeutic
695 target in Cancer. *Biochim Biophys Acta Rev Cancer* **1875** (2021).
696 15. K. Jaeger, *et al.*, Structural Basis for Allosteric Ligand Recognition in the Human CC
697 Chemokine Receptor 7. *Cell* **178**, 1222-1230.e10 (2019).
698 16. M. A. Hauser, D. F. Legler, Common and biased signaling pathways of the chemokine
699 receptor CCR7 elicited by its ligands CCL19 and CCL21 in leukocytes. *J Leukoc Biol* **99**,
700 869–882 (2016).
701 17. K. Schumann, *et al.*, immobilized chemokine fields and soluble chemokine gradients
702 cooperatively shape migration patterns of dendritic cells. *Immunity* **32**, 703–713 (2010).

703 18. M. Weber, *et al.*, Interstitial dendritic cell guidance by haptotactic chemokine gradients.
704 *Science* **339**, 328–332 (2013).
705 19. G. M. Hjortø, *et al.*, Differential CCR7 targeting in dendritic cells by three naturally
706 occurring CC-chemokines. *Front Immunol* **7**, 218657 (2016).
707 20. T. A. Kohout, *et al.*, Differential desensitization, receptor phosphorylation, β-arrestin
708 recruitment, and ERK1/2 activation by the two endogenous ligands for the CC
709 chemokine receptor 7. *Journal of Biological Chemistry* **279**, 23214–23222 (2004).
710 21. M. A. Byers, *et al.*, Arrestin 3 mediates endocytosis of CCR7 following ligation of CCL19
711 but not CCL21. *J Immunol* **181**, 4723–4732 (2008).
712 22. D. A. Zidar, J. D. Violin, E. J. Whalen, R. J. Lefkowitz, Selective engagement of G protein
713 coupled receptor kinases (GRKs) encodes distinct functions of biased ligands. *Proc Natl*
714 *Acad Sci U S A* **106**, 9649–9654 (2009).
715 23. Y. Yanagawa, K. Onoé, CCL19 induces rapid dendritic extension of murine dendritic
716 cells. *Blood* **100**, 1948–1956 (2002).
717 24. S. A. Luther, *et al.*, Differing activities of homeostatic chemokines CCL19, CCL21, and
718 CXCL12 in lymphocyte and dendritic cell recruitment and lymphoid neogenesis. *J*
719 *Immunol* **169**, 424–433 (2002).
720 25. Ulrike Haessler, Marco Pisano, Mingming Wu, M. A. Swartz, Dendritic cell chemotaxis in
721 3D under defined chemokine gradients reveals differential response to ligands CCL21
722 and CCL19. *Proc Natl Acad Sci U S A* **108**, 5614–5619 (2011).
723 26. A. S. Jørgensen, M. M. Rosenkilde, G. M. Hjortø, Biased signaling of G protein-coupled
724 receptors – From a chemokine receptor CCR7 perspective. *Gen Comp Endocrinol* **258**,
725 4–14 (2018).
726 27. X. Barros-Álvarez, *et al.*, The tethered peptide activation mechanism of adhesion
727 GPCRs. *Nature* **604**, 757–762 (2022).
728 28. Y. L. Liang, *et al.*, Dominant Negative G Proteins Enhance Formation and Purification of
729 Agonist-GPCR-G Protein Complexes for Structure Determination. *ACS Pharmacol Transl*
730 *Sci* **1**, 12–20 (2018).
731 29. A. S. Dixon, *et al.*, NanoLuc Complementation Reporter Optimized for Accurate
732 Measurement of Protein Interactions in Cells. *ACS Chem Biol* **11**, 400–408 (2016).
733 30. J. Duan, *et al.*, Cryo-EM structure of an activated VIP1 receptor-G protein complex
734 revealed by a NanoBiT tethering strategy. *Nat Commun* **11** (2020).
735 31. S. Maeda, *et al.*, Development of an antibody fragment that stabilizes GPCR/G-protein
736 complexes. *Nat Commun* **9** (2018).
737 32. Z. Shao, *et al.*, Molecular insights into ligand recognition and activation of chemokine
738 receptors CCR2 and CCR3. *Cell Discov* **8** (2022).
739 33. K. Liu, *et al.*, Structural basis of CXC chemokine receptor 2 activation and signalling.
740 *Nature* **585**, 135–140 (2020).
741 34. D. J. Wasilko, *et al.*, Structural basis for CCR6 modulation by allosteric antagonists. *Nat*
742 *Commun* **15** (2024).
743 35. Q. Zhou, *et al.*, Common activation mechanism of class A GPCRs. *Elife* **8** (2019).
744 36. L. Urvas, E. Kellenberger, Structural Insights into Molecular Recognition and Receptor
745 Activation in Chemokine-Chemokine Receptor Complexes. *J Med Chem* **66**, 7070–7085
746 (2023).

747 37. M. M. Rosenkilde, T. Benned-Jensen, T. M. Frimurer, T. W. Schwartz, The minor binding
748 pocket: A major player in 7TM receptor activation. *Trends Pharmacol Sci* **31**, 567–574
749 (2010).
750 38. A. S. Jørgensen, *et al.*, Biased Signaling of CCL21 and CCL19 Does Not Rely on N-
751 Terminal Differences, but Markedly on the Chemokine Core Domains and Extracellular
752 Loop 2 of CCR7. *Front Immunol* **10** (2019).
753 39. Q. Chen, *et al.*, Structures of rhodopsin in complex with G-protein-coupled receptor
754 kinase 1. *Nature* **595**, 600–605 (2021).
755 40. J. Duan, *et al.*, GPCR activation and GRK2 assembly by a biased intracellular agonist.
756 *Nature* **620**, 676–681 (2023).
757 41. A. Link, *et al.*, Fibroblastic reticular cells in lymph nodes regulate the homeostasis of
758 naive T cells. *Nat Immunol* **8**, 1255–1265 (2007).
759 42. H. E. Kato, *et al.*, Conformational transitions of a neurotensin receptor 1-Gi1 complex.
760 *Nature* **572**, 80–85 (2019).
761 43. Y. Gao, *et al.*, Structures of the Rhodopsin-Transducin Complex: Insights into G-Protein
762 Activation. *Mol Cell* **75**, 781-790.e3 (2019).
763 44. M. R. Britschgi, A. Link, T. K. A. Lissandrin, S. A. Luther, Dynamic modulation of CCR7
764 expression and function on naive T lymphocytes in vivo. *J Immunol* **181**, 7681–7688
765 (2008).
766 45. S. Nandagopal, D. Wu, F. Lin, Combinatorial guidance by CCR7 ligands for T lymphocytes
767 migration in co-existing chemokine fields. *PLoS One* **6** (2011).
768 46. K. Schaeuble, *et al.*, Perivascular Fibroblasts of the Developing Spleen Act as LTα1β2-
769 Dependent Precursors of Both T and B Zone Organizer Cells. *Cell Rep* **21**, 2500–2514
770 (2017).
771 47. K. Y. Chen, *et al.*, Inflammation switches the chemoattractant requirements for naive
772 lymphocyte entry into lymph nodes. *Cell* **188**, 1019-1035.e22 (2025).
773 48. A. Goehring, *et al.*, Screening and large-scale expression of membrane proteins in
774 mammalian cells for structural studies. *Nat Protoc* **9**, 2574–2585 (2014).
775 49. P. A. Longo, J. M. Kavran, M. S. Kim, D. J. Leahy, Transient mammalian cell transfection
776 with polyethylenimine (PEI). *Methods Enzymol* **529**, 227–240 (2013).
777 50. A. Wellner, *et al.*, Rapid generation of potent antibodies by autonomous hypermutation
778 in yeast. *Nat Chem Biol* **17**, 1057–1064 (2021).
779 51. N. Tsutsumi, *et al.*, Atypical structural snapshots of human cytomegalovirus GPCR
780 interactions with host G proteins. *Sci Adv* **8** (2022).
781 52. N. Tsutsumi, *et al.*, Structure of the thrombopoietin-MPL receptor complex is a
782 blueprint for biasing hematopoiesis. *Cell* **186**, 4189-4203.e22 (2023).
783 53. A. Dukkipati, H. H. Park, D. Waghray, S. Fischer, K. C. Garcia, BacMam system for high-
784 level expression of recombinant soluble and membrane glycoproteins for structural
785 studies. *Protein Expr Purif* **62**, 160–170 (2008).
786 54. M. Schorb, I. Haberbosch, W. J. H. Hagen, Y. Schwab, D. N. Mastronarde, Software tools
787 for automated transmission electron microscopy. *Nat Methods* **16**, 471–477 (2019).
788 55. A. Punjani, J. L. Rubinstein, D. J. Fleet, M. A. Brubaker, cryoSPARC: algorithms for rapid
789 unsupervised cryo-EM structure determination. *Nat Methods* **14**, 290–296 (2017).

790 56. T. Bepler, *et al.*, Positive-unlabeled convolutional neural networks for particle picking in
791 cryo-electron micrographs. *Nat Methods* **16**, 1153–1160 (2019).
792 57. R. Sanchez-Garcia, *et al.*, DeepEMhancer: a deep learning solution for cryo-EM volume
793 post-processing. *Commun Biol* **4** (2021).
794 58. D. Asarnow, E. Palovcak, Y. Cheng, asarnow/pyem: UCSF pyem v0.5. [Preprint] (2019).
795 Available at: https://doi.org/10.5281/zenodo.3576630.
796 59. J. Abramson, *et al.*, Accurate structure prediction of biomolecular interactions with
797 AlphaFold 3. *Nature* **630**, 493–500 (2024).
798 60. D. Liebschner, *et al.*, Macromolecular structure determination using X-rays, neutrons
799 and electrons: recent developments in Phenix. *Acta Crystallogr D Struct Biol* **75**, 861–
800 877 (2019).
801 61. P. Emsley, B. Lohkamp, W. G. Scott, K. Cowtan, Features and development of Coot. *Acta*
802 *Crystallogr D Biol Crystallogr* **66**, 486–501 (2010).
803 62. E. F. Pettersen, *et al.*, UCSF ChimeraX: Structure visualization for researchers,
804 educators, and developers. *Protein Sci* **30**, 70–82 (2021).
805 63. S. Jo, T. Kim, V. G. Iyer, W. Im, CHARMM-GUI: a web-based graphical user interface for
806 CHARMM. *J Comput Chem* **29**, 1859–1865 (2008).
807 64. J. Lee, *et al.*, CHARMM-GUI Input Generator for NAMD, GROMACS, AMBER, OpenMM,
808 and CHARMM/OpenMM Simulations Using the CHARMM36 Additive Force Field. *J*
809 *Chem Theory Comput* **12**, 405–413 (2016).
810 65. E. L. Wu, *et al.*, CHARMM-GUI Membrane Builder toward realistic biological membrane
811 simulations. *J Comput Chem* **35**, 1997–2004 (2014).
812 66. E. Mayol, *et al.*, HomolWat: a web server tool to incorporate "homologous" water
813 molecules into GPCR structures. *Nucleic Acids Res* **48**, W54–W59 (2020).
814 67. D. C. Bas, D. M. Rogers, J. H. Jensen, Very fast prediction and rationalization of pKa
815 values for protein-ligand complexes. *Proteins* **73**, 765–783 (2008).
816 68. B. R. Brooks, *et al.*, CHARMM: the biomolecular simulation program. *J Comput Chem*
817 **30**, 1545–1614 (2009).
818 69. M. A. Lomize, I. D. Pogozheva, H. Joo, H. I. Mosberg, A. L. Lomize, OPM database and
819 PPM web server: resources for positioning of proteins in membranes. *Nucleic Acids Res*
820 **40** (2012).
821 70. J. Huang, *et al.*, CHARMM36m: an improved force field for folded and intrinsically
822 disordered proteins. *Nat Methods* **14**, 71–73 (2017).
823 71. D. Van Der Spoel, *et al.*, GROMACS: fast, flexible, and free. *J Comput Chem* **26**, 1701–
824 1718 (2005).
825 72. G. Bussi, D. Donadio, M. Parrinello, Canonical sampling through velocity rescaling. *J*
826 *Chem Phys* **126** (2007).
827 73. H. J. C. Berendsen, J. P. M. Postma, W. F. Van Gunsteren, A. Dinola, J. R. Haak,
828 Molecular dynamics with coupling to an external bath. *J Chem Phys* **81**, 3684–3690
829 (1984).
830 74. M. Bernetti, G. Bussi, Pressure control using stochastic cell rescaling. *J Chem Phys* **153**
831 (2020).
832 75. B. Hess, P-LINCS: A Parallel Linear Constraint Solver for Molecular Simulation. *J Chem*
833 *Theory Comput* **4**, 116–122 (2008).

76. T. Darden, D. York, L. Pedersen, Particle mesh Ewald: An N·log(N) method for Ewald sums in large systems. *J Chem Phys* **98**, 10089–10092 (1993).
77. N. Michaud-Agrawal, E. J. Denning, T. B. Woolf, O. Beckstein, MDAnalysis: a toolkit for the analysis of molecular dynamics simulations. *J Comput Chem* **32**, 2319–2327 (2011).
78. J. D. Hunter, Matplotlib: A 2D graphics environment. *Comput Sci Eng* **9**, 90–95 (2007).
79. F. Pedregosa, *et al.*, Scikit-learn: Machine Learning in Python. *Journal of Machine Learning Research* **12**, 2825–2830 (2011).

843 **Materials and Data availability**

844 • All unique/stable reagents generated in this study are available from the corresponding author
845 upon formal publication by request, provided there is no licensing issue.

846 • All standardized datasets are publicly available as follows. The cryo-EM maps (the model
847 coordinates) have been deposited in the Electron Microscopy Data Bank (Protein Data Bank)
848 under accession codes of EMD-66874 (PDB: 9XHH) and EMD-66875 (PDB: 9XHI) for CCL19-CCR7-
849 G_i-scFv16 and CCL21-CCR7-G_i-scFv16, respectively.

850 • All data were analyzed with standard or reported programs and packages, as detailed in the
851 Methods. This paper does not report original code. Any additional information required to
852 reanalyze the data reported in this paper is available from the corresponding author upon
853 reasonable request following formal publication.

854

855 **Acknowledgement**

856 We thank the members of Cellular and Structural Physiology Laboratory (CeSPL) for daily
857 scientific discussion and Ms. Miho Sasaki for supporting the research. This work was supported
858 by the Japan Society for the Promotion of Science (JSPS) KAKENHI (JP24K01965 and JP24K21935
859 to N.T. and JP20H00451 to Y.F). The MD simulations were performed using the TSUBAME4.0
860 supercomputer at Institute of Science Tokyo.

861 **Fig. 1**

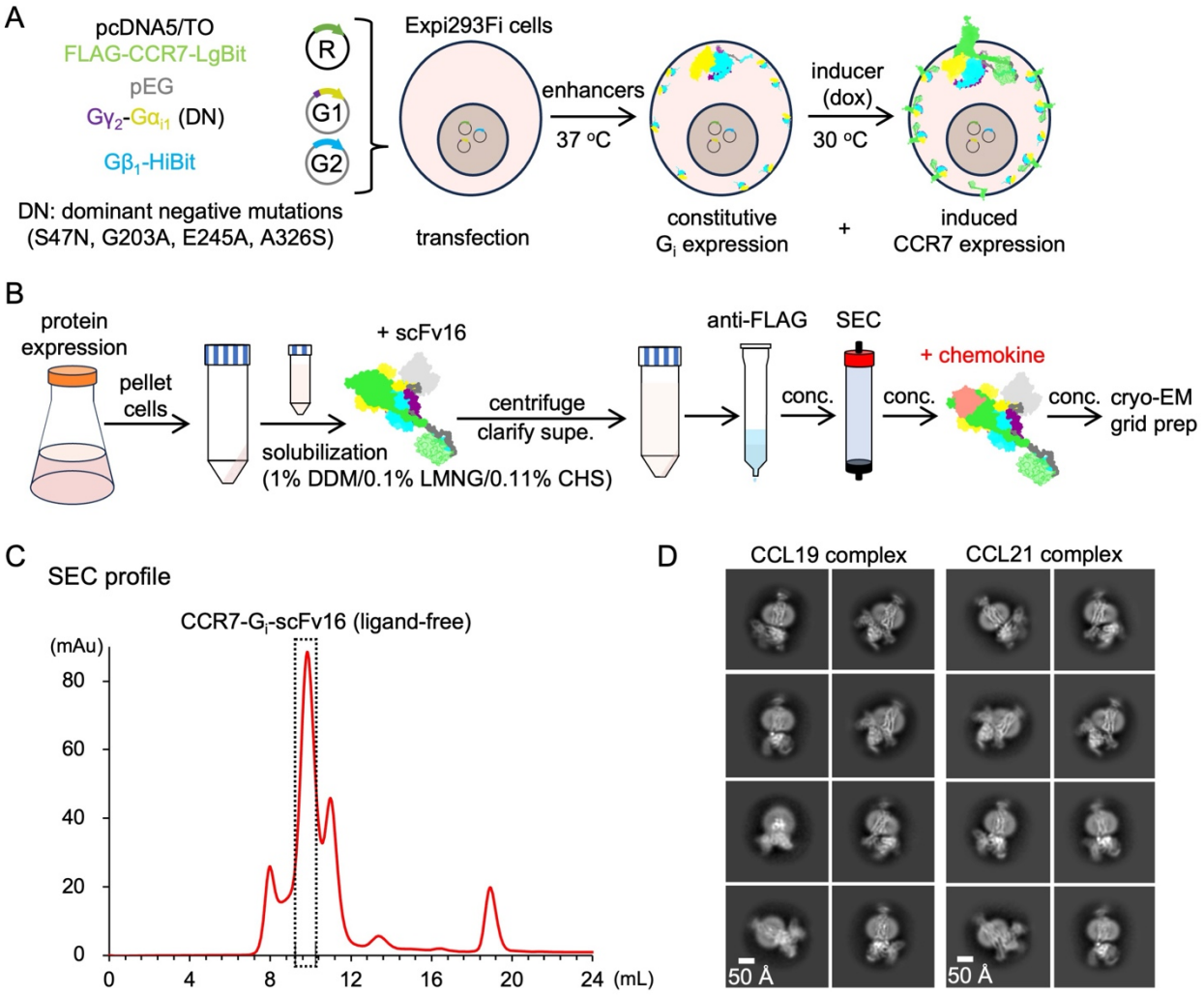

862

863 **Fig. 1 | Temporally controlled mammalian expression of the CCR7-G_i complexes for cryo-EM**
864 **analysis.**
865 (A) Schematic representation of the temporally controlled expression system in inducible
866 Expi293F cells. Plasmids encoding FLAG-CCR7-LgBiT (R; inducible, pcDNA5/TO) and G_i
867 heterotrimer components [constitutive, pEG; Gγ2-$G\alpha_{i1}$(DN) (G1) and $G\beta_1$-HiBiT (G2)] are co-
868 transfected. Cells are cultured at 37°C for constitutive G_i expression, followed by induction with
869 doxycycline (dox) and temperature shift to 30°C for induced CCR7 expression and sustained G_i
870 expression. DN denotes dominant negative mutations (S47N, G203A, E245A, A326S) in $G\alpha_{i1}$. (B)
871 Workflow for the purification of the CCR7-G_i-scFv16 complexes, highlighting the strategy of
872 purifying the apo-complex followed by the addition of chemokines. (C) Size-exclusion
873 chromatography (SEC) profile of the ligand-free CCR7-G_i-scFv16 complex. The peak fraction used
874 for subsequent steps is indicated by the dashed box. Chemokines are added to this sample for
875 cryo-EM analysis. (D) Selected 2D class averages (scale bar 50 Å) of the CCL19-CCR7-G_i-scFv16
876 complex (left) and the CCL21-CCR7-G_i-scFv16 complex (right).

877 **Fig. 2**

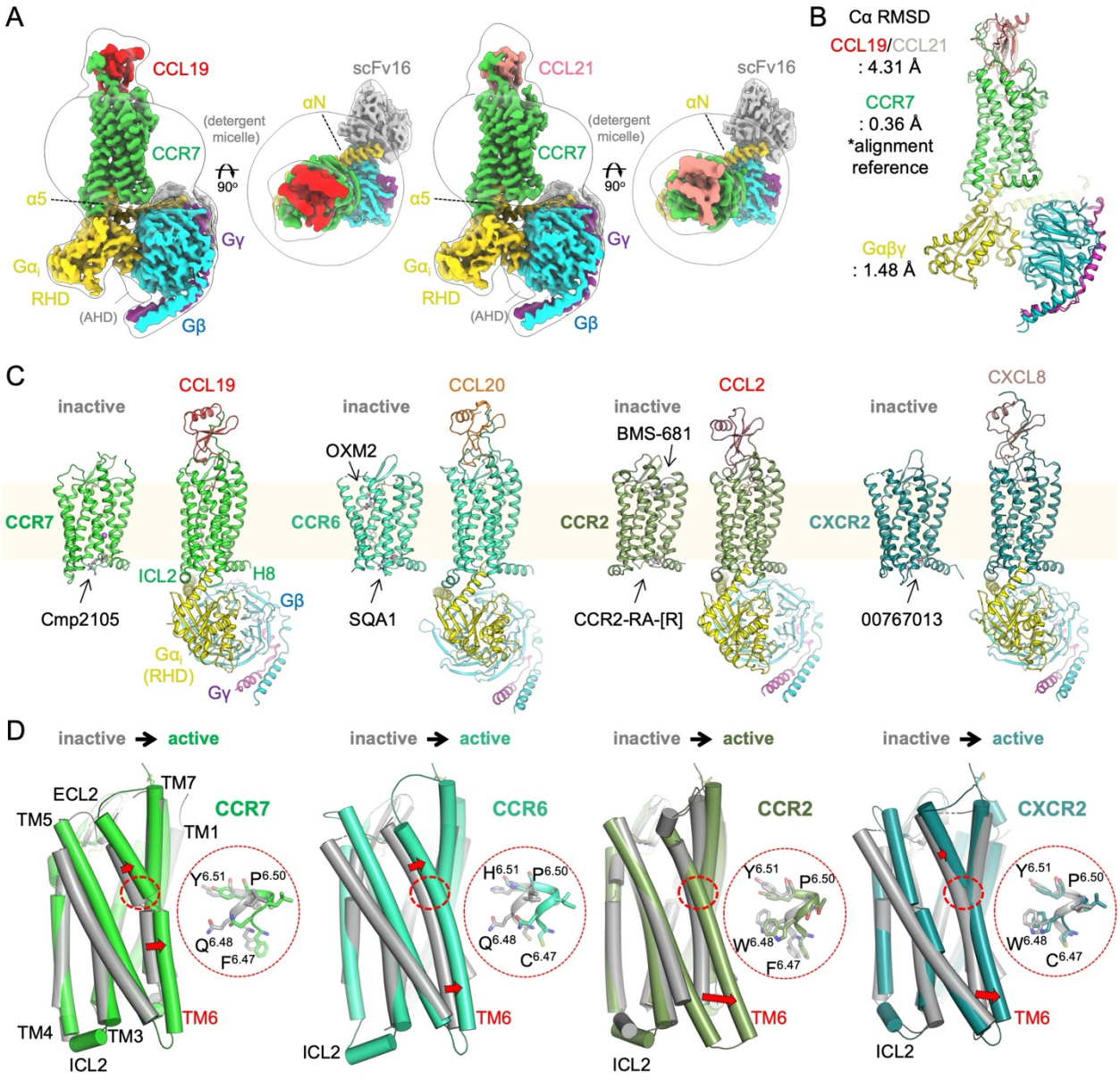

878

879 **Fig. 2 | Structures of CCR7-G_i complexes and global conformational changes upon Activation.**
880 (A) Cryo-EM maps of the CCL19-CCR7-G_i-scFv16 (left) and CCL21-CCR7-G_i-scFv16 (right)
881 complexes. Structures are shown in side views and top views. Color coding: CCL19 (red), CCL21
882 (orange), CCR7 (green), $G\alpha_i$ (yellow; RHD: Ras Homology Domain, AHD: Alpha Helical Domain),
883 Gβ (cyan), Gγ (purple), scFv16 (gray). (B) Superposition of the ribbon models of the CCL19-bound
884 and CCL21-bound complexes. Alignment was performed based on CCR7. Cα root-mean-square
885 deviations (RMSD) are indicated for the chemokines, CCR7, and Gαβγ. (C) Comparison of active
886 and inactive state structures of CCR7 and related chemokine receptors. Top row: Overall
887 structures showing G protein coupling or antagonist/inhibitor binding.
888 *Caption continued on the next page.*

889 **Fig. 2** *continued*:
890 Structures include inactive CCR7 bound to Cmp2105 (PDB: 6QZH); active CCR7 bound to CCL19
891 (this study); inactive CCR6 bound to OXM2 and SQA1 (PDB: 9D3E); active CCR6 bound to CCL20
892 (PDB: 6WWZ); inactive CCR2 bound to BMS-681 and CCR2-RA-[R] (PDB: 5T1A); active CCR2 bound
893 to CCL2 (PDB: 7XA3); inactive CXCR2 bound to 00767013 (PDB: 6LFL); active CXCR2 bound to
894 CXCL8 (PDB: 6LFO). (D) Superimposition of the inactive and active structures of chemokine
895 receptors. Inactive states are shown in gray, and active states are separately colored. Red arrows
896 indicate the outward movement of TM6. The region corresponding to the conserved CWxP motif
897 (FQxP in CCR7 and CCR6) is indicated by red dashed circles and shown on the right.

Fig. 3

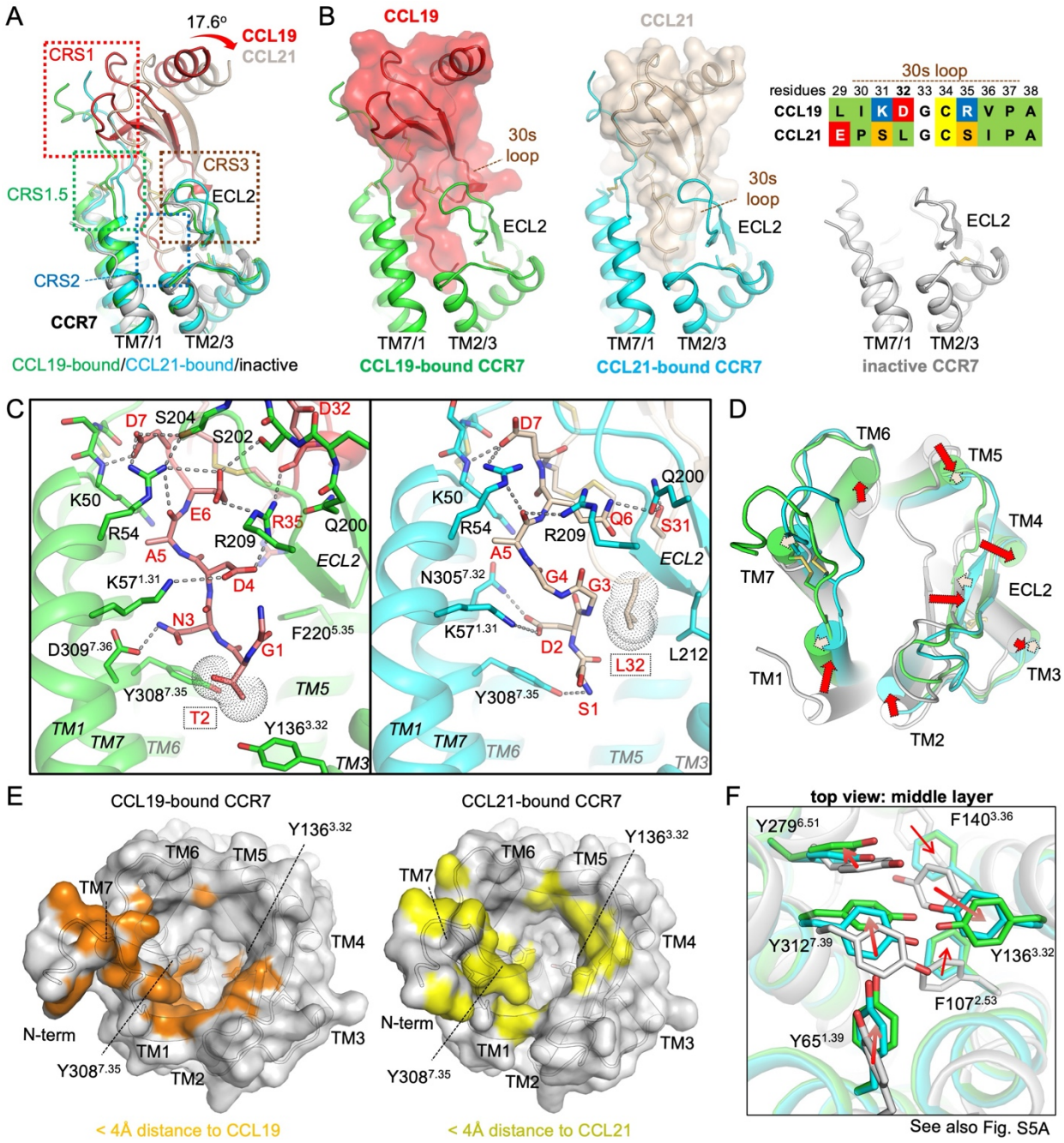

Fig. 3 | Distinct ligand binding modes of CCL19 and CCL21 at CCR7.
(A) Superposition of the CCL19-CCR7 (red-green) and CCL21-CCR7 (orange-cyan) complexes, highlighting the 17.6° rotation of CCL21 relative to CCL19. The chemokine recognition sites (CRS1, CRS1.5, CRS2, CRS3) are indicated by the dashed boxes. (B) Divergent interactions at the CRS3 interface. CCL19-CCR7 (left), CCL21-CCR7 (center), and inactive CCR7 (right, gray) are shown side-by-side to compare the extracellular structures especially the interaction between the chemokine 30s loop and CCR7-ECL2 at CRS3. A sequence alignment of the 30s loops of CCL19 and CCL21 is displayed on top of the inactive CCR7 structure. *Caption continued on the next page.*

908 **Fig. 3** *continued*:
909 (C) Conserved and distinct interactions at the CRS2/3 interfaces. Close-up views of the chemokine
910 N-terminus penetration into the orthosteric binding pocket for CCL19 (left) and CCL21 (right). Key
911 interacting residues are shown as sticks, and polar interactions are indicated by dashed lines. (D)
912 Ligand-specific conformational changes in the extracellular TMs and ECL2. Superposition of the
913 CCL19-bound and CCL21-bound CCR7 structures with the inactive CCR7 structure, highlighting
914 the conformational differences induced by the distinct ligand binding modes. Red arrows indicate
915 conformational shifts from the inactive state to the CCL21-bound state, and peach arrows
916 indicate the further shifts observed in the CCL19-bound state. (E) Chemokine footprints on the
917 CCR7 binding pocket. Top views of the CCR7 surface colored according to the distance to CCL19
918 (left) or CCL21 (right). Residues within 4 Å of the respective chemokine are colored. $Y136^{3.32}$ and
919 $Y308^{7.35}$ are shown as markers. (F) Rearrangement of the aromatic cluster in the middle layer of
920 the TM bundle. Close-up view of the superimposed structures showing the distinct
921 conformations of $Y65^{1.39}$, $F107^{2.53}$, $Y136^{3.32}$, $Y279^{6.51}$, $Y308^{7.35}$, and $Y312^{7.39}$ in the CCL19-bound
922 and CCL21-bound states compared to the inactive CCR7 (PDB: 6QZH). See also Fig. S5.

923 **Fig. 4**

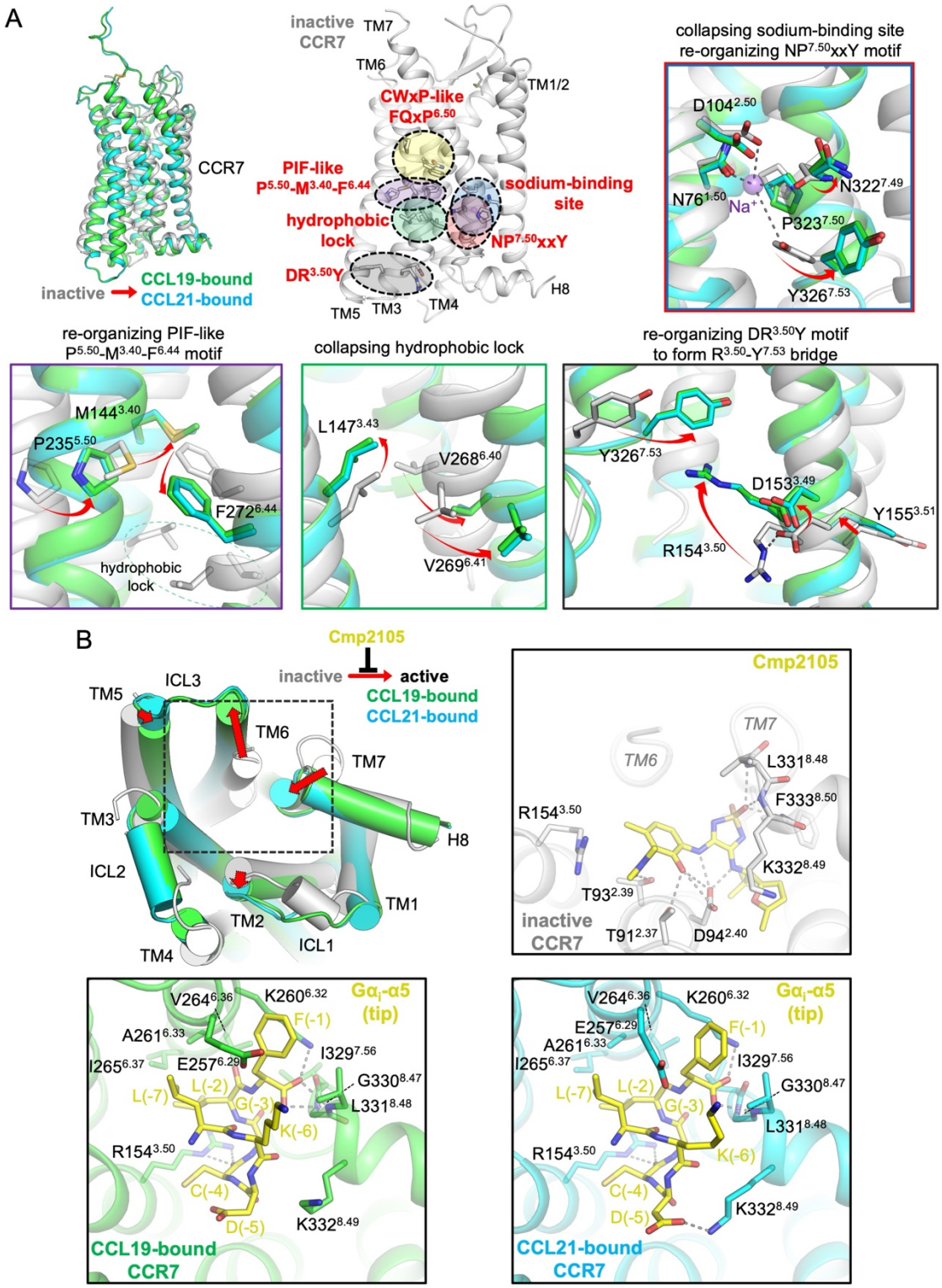

924

925 *Fig. 4 caption on the next page.*

926 **Fig. 4 | Structural basis of CCR7 activation.**
927 (A) Conserved GPCR activation motifs and conformational changes in CCR7. Top left:
928 Superposition of inactive CCR7 (gray) and active CCR7 (CCL19-bound in green, CCL21-bound in
929 cyan). Top center: Mapping of the key GPCR activation motifs highlighted on the inactive CCR7
930 structure. Other panels show close-up views of the reorganization of the motifs upon activation.
931 Key residues are shown as sticks. Arrows indicate the direction of movement from the inactive
932 to the active state. Top right: Collapse of the sodium-binding site and reorganization of the
933 $NP^{7.50}$xxY motif. Bottom left: Reorganization of the PIF-like $P^{5.50}$-$M^{3.40}$-$F^{6.44}$ motif upstream of the
934 hydrophobic lock. Bottom center: Collapse of the hydrophobic lock. Bottom right: Reorganization
935 of the $DR^{3.50}$Y motif and formation of a G protein-binding interface with the $R^{3.50}$-$Y^{7.53}$ bridge. (B)
936 G protein coupling and comparison with the antagonist-bound state. Top left: Superposition of
937 active CCR7 (CCL19-bound in green, CCL21-bound in cyan) and inactive CCR7 bound to Cmp2105
938 (gray). The inactive-to-active TM movements, which are generally conserved between the CCL19-
939 bound and CCL21-bound states in complex with G_i, are indicated by red arrows. Top right: Close-
940 up view showing how Cmp2105 (yellow sticks) occupies the G protein binding site in the inactive
941 CCR7. Cmp2105 also inhibits the inactive-to-active conformational transition. Bottom panels:
942 Detailed interactions between the $G\alpha_i$ α5 helix (yellow, C-terminal 7 residues) and the CCR7
943 intracellular cavity in the CCL19-bound (left) and CCL21-bound (right) complexes. Key residues
944 involved in the interaction are shown as sticks, and polar contacts are indicated by dashed lines.

945 **Fig. 5**

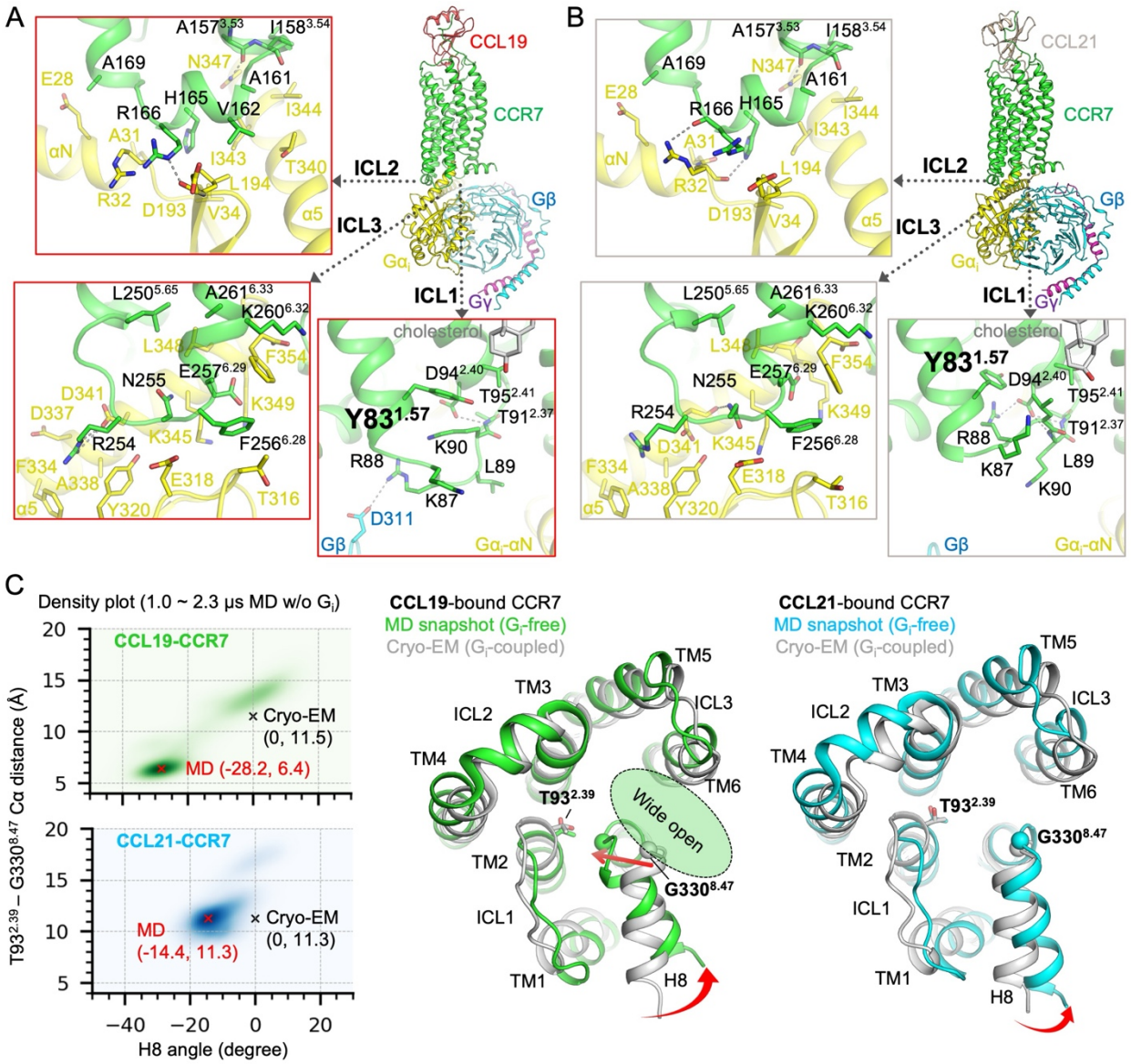

946

947 **Fig. 5 | Conserved G_i interface but distinct intracellular dynamics revealed by MD simulations**
948 The G_i binding interface of the (A) CCL19-CCR7-G_i and (B) CCL21-CCR7-G_i complexes. Overall
949 views are displayed on top right, where zoomed-in boxes highlight the interfaces centering ICL2
950 (top left), ICL3 (bottom left), and ICL1 (bottom right). The contacting residues within 4 Å distance
951 are shown as sticks, and polar interactions are shown by dashed lines. Cholesterol molecules near
952 ICL1 are shown as gray sticks. (C) Comparison of the H8 orientation after the G_i free MD
953 simulations between CCL19-bound (green) and CCL21-bound (cyan) CCR7. Left: Probability
954 density plot of the H8 angle versus the $T93^{2.39}$-$G330^{8.47}$ distance. Data were calculated from six
955 independent 2.3 μs G_i-free MD simulations, excluding the first 1 μs of each run as a relaxation
956 period. See Fig. S8C for the definition of the H8 angle. The angles and the distances from the cryo-
957 EM models and the MD density peak are indicated by black ('x') and red ('x') markers with
958 corresponding text, respectively. *Caption continued on the next page.*

959 **Fig. 5** *continued*:
960 Right: Superposition of the Gi free MD snapshot and the Gi-coupled cryo-EM structure. The
961 residues used for the distance measurement in the density plot, $T93^{2.39}$ and $G330^{8.47}$, are shown
962 as sticks and spheres, respectively. The larger degree of the H8 rotation and the consequent
963 insertion of the TM7-H8 loop open the gap between H8 and TM6 in the CCL19-bound CCR7
964 compared to the CCL21-bound CCR7.

Fig. 6

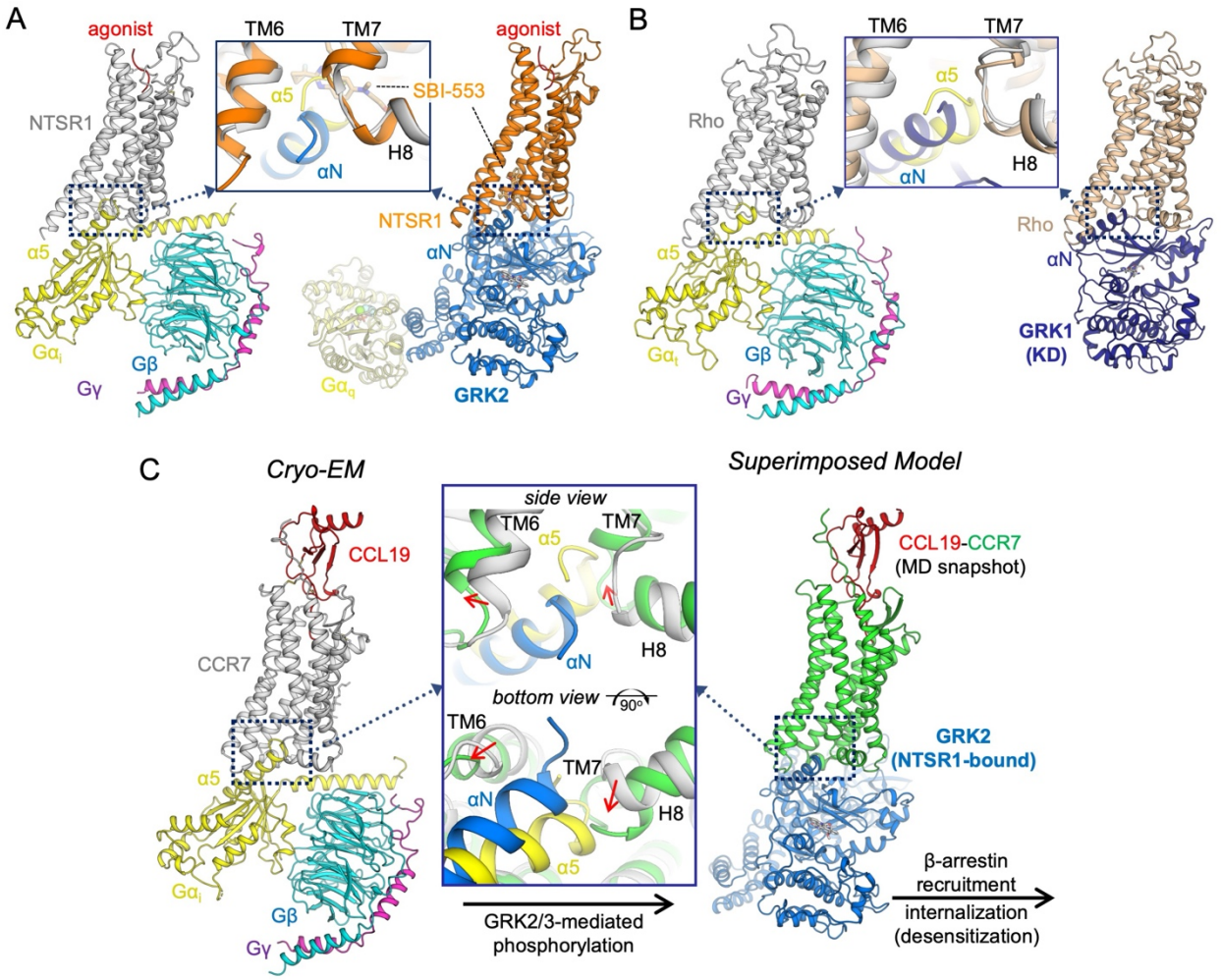

Fig. 6 | Comparison of G protein and GRK binding modes and a structural model for CCR7 biased agonism.

(A) Cryo-EM structures of Neurotensin Receptor 1 (NTSR1) in complex with G_i (PDB: 6OS9, left) and GRK2 (PDB: 8JPB, right). The zoomed-in inset shows a superposition of the two complexes, aligned on the receptor (NTSR1), to directly compare the binding modes of the C-terminal α5 helix of the Gα subunit (yellow) and the N-terminal αN helix of the GRK (blue). (B) Cryo-EM structures of Rhodopsin (Rho) in complex with G_t (PDB: 6OY9, left) and GRK1 (PDB: 7MTA, right). The zoomed-in inset shows a superposition of the Rho-G_t and Rho-GRK1 complexes, aligned on the receptor (Rhodopsin), to compare the effector helices. Both (A) and (B) highlight that while both effectors engage the receptor's cytoplasmic core, the GRK-αN helix exhibits a shallower insertion than the Gα-α5 helix (yellow) and follows a distinct trajectory, exiting through the interface formed by TM6, TM7, and H8.

Caption continued on the next page.

982 **Fig. 6** *continued*:
983 (C) Proposed structural model for the biased activation of GRK2/3 by CCR7. Cryo-EM structure of
984 the CCL19-CCR7-G_i complex (this study, left) and a superimposed model illustrating the proposed
985 mechanism of CCR7-GRK2 engagement (right). The model was generated by superimposing a
986 representative "open" conformation of CCL19-CCR7 (green), derived from MD simulations (Fig.
987 5C and S8B), onto the NTSR1 receptor of the cryo-EM NTSR1-GRK2 complex (PDB 8JPB). The
988 zoomed-in inset compares the G_i-bound state (gray helices, Gα-α5 in yellow) with the modeled
989 'open' GRK-bound state (green helices, GRK-αN in blue). This illustrates that the "open" state,
990 stabilized by CCL19-induced H8 dynamics after G protein dissociation, creates a wide gap
991 between TM6 and H8, which appears sterically complementary to accommodate the GRK-αN
992 helix. This simple model suggests that CCL19-induced dynamics selectively favor this "open"
993 ensemble, facilitating efficient GRK2/3 recruitment and robust β-arrestin signaling.